



LIBRARY Michigan State University

This is to certify that the

thesis entitled

Development and Validation of a Computer Model of the Equine Tarsal Joint

presented by

Adam Karekin Arabian

has been accepted towards fulfillment of the requirements for

Masters degree in Mechanical Engineering

Date April 28, 2000

MSU is an Affirmative Action/Equal Opportunity Institution

PLACE IN RETURN BOX to remove this checkout from your record. TO AVOID FINES return on or before date due. MAY BE RECALLED with earlier due date if requested.

DATE DUE	DATE DUE	DATE DUE
NOV2 1 9 2002		
<u> </u>		

11/00 c/CIRC/DateDue.p65-p.14

DEVELOPMENT AND VALIDATION OF A COMPUTER MODEL OF THE EQUINE TARSAL JOINT

By

Adam Karekin Arabian

A THESIS
Submitted To
Michigan State University
in partial fulfillment of the requirements
for the degree of

MASTER OF SCIENCE

Department of Mechanical Engineering

2000

ABSTRACT

DEVELOPMENT AND VALIDATION OF A COMPUTER MODEL OF THE EQUINE TARSAL JOINT

By

Adam Karekin Arabian

The equine tarsal joint is the site of a high percentage of hindlimb lameness cases seen in veterinary medicine. In order to better understand the defining morphology of the tarsal joint, a computer model of the joint was developed. Computerized tomography (CT) scans were taken of the disarticulated bones of the joint and edge detection was performed on the resultant images. The edge data were translated into a format readable by an engineering design software package, and the three-dimensional points were used in the definition of solid models of the bones of the tarsal joint. As an example of the model's utility, it was used to evaluate the generally held assumption that all motion of the tarsal joint occurs at the articulation of the tibia and talus. The motion of the tibia with respect to the metatarsus was determined based on the curvature and orientation of the talar trochlea, and compared to the motion determined from experimental kinematic analysis. The results indicated that the tibia demonstrated motion not fully explainable by the morphology of the talus, and hence it was determined that some amount of tarsal joint motion must occur at the intertarsal and tarsometatarsal joints.

Acknowledgments

I would like to thank my supervisors, Professor Hilary M. Clayton of the Michigan State University Department of Veterinary Medicine, and Professor Ranjan Mukherjee of the Michigan State University Department of Mechanical Engineering for their support and guidance during the course of this research and the writing of this thesis. My sincerest appreciation is also expressed to Joel Lanovaz, Manager of the McPhail Lab for Equine Sports Medicine, for his technical assistance and support throughout this research.

I would also like to express my gratitude to my friends and family, without whose support I could not have completed this research.

This research was supported in part by the Mary Anne McPhail Endowment, to which I am indebted

Table of Contents

LIST OF TABLES	vi
List of Figures	vii
GLOSSARY	ix
1. Introduction	1
1.1. HISTORICAL PERSPECTIVE	1
1.2. EQUINE BIOMECHANICS	4
1.3. COMPUTER MODELS IN BIOMECHANICS	5
1.4. RESEARCH OBJECTIVES	7
2. ANATOMY OF THE EQUINE HINDLIMB	8
2.1. STRUCTURE AND MORPHOLOGY	8
2.2. ANATOMY, MOTION, AND PATHOLOGY OF THE TARSAL JOINT	10
2.2.1. Bones of the Tarsal Joint	10
2.2.2. Intertarsal Joints	12
2.2.3. Pathologies of the Tarsal Joint	13
3. METHOD OF INVESTIGATION	15
3.1. COLLECTION AND PREPARATION OF ARTICULATED SPECIMEN OF THE TARSAL JOINT	15
3.2. COMPUTERIZED TOMOGRAPHY SCAN OF ARTICULATED TARSAL JOINT	15
3.3. PREPARATION OF DISARTICULATED TARSAL BONES	16
3.4. COMPUTERIZED TOMOGRAPHY SCAN OF DISARTICULATED TARSAL BONES	18
3.5. IMAGE PROCESSING	19
3.6. EDGE DETECTION ALGORITHM	20

3.7. CREATION OF THE SOLID MODEL	4
3.8. DEVELOPMENT OF TOOL FOR MODEL VISUALIZATION	9
3.9. MODEL VALIDATION BY VOLUMETRIC MEASUREMENTS	2
3.10. APPLICATION OF MODEL	3
4. RESULTS42	2
4.1. COMPUTER MODELS OF THE BONES OF THE TARSAL JOINT	2
4.1.1. Tibia	3
4.1.2. Talus	4
4.1.3. Calcaneus	5
4.1.4. Central and Third Tarsal Bones	6
4.1.5. First and Second Tarsal Bone and Fourth Tarsal Bone	8
4.1.6. Metatarsus	9
4.2. RESULTS OF VOLUMETRIC MEASUREMENTS	0
4.3. APPLICATION OF MODEL TO PREDICTION OF MOTION OF THE TARSAL JOINT	1
4.3.1. Stance phase	4
Swing Phase	7
5. DISCUSSION	9
5.1. MODELING TECHNIQUES	9
5.2. MODEL VALIDATION BY VOLUMETRIC MEASUREMENTS	4
5.3. APPLICATION OF MODEL IN THE EVALUATION OF TARSAL JOINT KINEMATICS	5
6. CONCLUSION AND FUTURE STUDIES70)
REFERENCES	3

List of Tables

Table 1. Nul	ABER OF CROSS	S SECTIONAL CUR	VES AND	SURFACES IN	COMPUTER	MODEL OF	ZEACH BONE	. 43
--------------	---------------	-----------------	---------	-------------	----------	----------	------------	------

TABLE 2. COMPARISON OF SPECIMEN VOLUMES AND CALCULATED VOLUMES OF COMPUTER MODELS 50

List of Figures

FIGURE 1.	COMPARISON OF ANATOMY BETWEEN THE HUMAN LEG AND EQUINE HINDLIMB (EQUINE SPECIFIC	С
	NAMES IN PARENTHASES)	8
FIGURE 2.	RIGHT TARSAL JOINT, CRANIAL VIEW	ا0
FIGURE 3.	RIGHT TARSAL JOINT, MEDIAL VIEW	10
FIGURE 4.	RIGHT TARSAL JOINT, CRANIAL VIEW	12
FIGURE 5.	RIGHT TARSAL JOINT, MEDIAL VIEW	2
FIGURE 6.	FINAL DESIGN OF COORDINATE APPARATUS	8
FIGURE 7.	CROSS SECTIONAL IMAGE OF THE TARSUS TRANSECTING THE CALCANEUS AND TIBIOTARSAL	
	JOINT	23
FIGURE 8.	CROSS SECTIONAL OF IMAGE AFTER APPLYING THE CANNY EDGE DETECTION ALGORITHM	
	(SCHNUCK, 1986)	!3
FIGURE 9.	CROSS SECTION CURVES USED FOR LOFT DEFINITION ON THE METATARSUS	:7
FIGURE 10.	RESULTANT SURFACE FROM THE LOFTING TECHNIQUE ON THE METATARSUS	:7
Figure 11.	CROSS SECTION AND RAIL CURVES USED FOR SURFACE DEFINITION ON THE CALCANEUS 2	28
Figure 12.	RESULTANT SURFACE FROM THE MESH OF CURVES TECHNIQUE ON THE CALCANEUS	28
FIGURE 13.	CURVE GRID USED FOR SURFACE DEFINITION ON PROXIMAL SURFACE OF THE METATARSUS. 2	!9
Figure 14.	RESULTANT SURFACE FROM THE SURFACE STITCHING TECHNIQUE ON THE METATARSUS 2	:9
FIGURE 15.	DIRECTX ANIMATION VIEWER	1
FIGURE 16.	ROTATIONAL AXIS DEFINITIONS USED IN ANALYSIS OF JOINT ANGLES	4
Figure 17.	MARKER LOCATIONS USED ON THE TIBIA FOR KINEMATIC DATA COLLECTION	5
FIGURE 18.	MARKER LOCATIONS USED ON THE METATARSUS FOR KINEMATIC DATA COLLECTION 3	5
FIGURE 19.	EXPERIMENTAL SETUP FOR KINEMATIC DATA COLLECTION	6
FIGURE 20.	METATARSAL, TALAR, AND TIBIAL COORDINATE SYSTEM DEFINITIONS FOR MODEL BASED	
	ANALYSIS	8
FIGURE 21.	DISTAL END OF TIBIA	.3
FIGURE 22.	COMPUTER MODEL OF DISTAL TIBIA	3
FIGURE 23.	TALUS SPECIMEN4	4

FIGURE 24.	COMPUTER MODEL OF TALUS	44
FIGURE 25.	CALCANEUS SPECIMEN	45
FIGURE 26.	COMPUTER MODEL OF CALCANEUS	45
FIGURE 27.	CENTRAL TARSAL BONE SPECIMEN	46
FIGURE 28.	COMPUTER MODEL OF CENTRAL TARSAL BONE	46
Figure 29.	THIRD TARSAL BONE SPECIMEN	47
FIGURE 30.	COMPUTER MODEL OF THIRD TARSAL BONE	47
FIGURE 31.	FIRST AND SECOND TARSAL BONE SPECIMEN	48
FIGURE 32.	COMPUTER MODEL OF FIRST AND SECOND TARSAL BONE	48
FIGURE 33.	FOURTH BONE SPECIMEN	48
FIGURE 34.	COMPUTER MODEL OF FOURTH TARSAL BONE	48
FIGURE 35.	PROXIMAL END OF METATARSUS SPECIMEN	49
FIGURE 36.	COMPUTER MODEL OF PROXIMAL METATARSUS	49
FIGURE 37.	PREDICTED ABDUCTION/ADDUCTION ANGLE VS. FLEXION/EXTENSION ANGLE BASED ON	
	ANALYSIS OF MORPHOLOGY OF TALUS AND TIBIA	52
FIGURE 38.	PREDICTED INTERNAL/EXTERNAL ROTATION ANGLE VS. FLEXION/EXTENSION ANGLE BASE	D
	ON ANALYSIS OF MORPHOLOGY OF TALUS AND TIBIA	53
FIGURE 39.	FLEXION/EXTENSION ANGLE VS. ABDUCTION/ADDUCTION FOR STANCE PHASE	54
FIGURE 40.	FLEXION/EXTENSION VS. INTERNAL/EXTERNAL ROTATION FOR STANCE PHASE	55
FIGURE 41.	FLEXION/EXTENSION VS. ABDUCTION/ADDUCTION ANGLE FOR SWING PHASE	57
FIGURE 42.	FLEXION/EXTENSION VS. INTERNAL/EXTERNAL ROTATION FOR SWING PHASE	58
FIGURE 43.	SECTION OF ORIGINAL IMAGE	64
FIGURE 44.	ROBERTS EDGE DETECTION OF SELECTED REGION	64
FIGURE 45.	CANNY EDGE DETECTION OF SELECTED REGION	64
FIGURE 46.	SECTION OF ORIGINAL IMAGE	64
FIGURE 47.	SOBEL EDGE DETECTION OF SELECTED REGION	64
FIGURE 48.	CANNY EDGE DETECTION OF SELECTED REGION	64

Glossary

Internal Positive rotation about the axis defined by the long

Rotation axis of the bone

Abduction Increase in segment angle with respect to the midline

of the body

Adduction Decrease in segment angle with respect to the midline

of the body

Biomechanics The application of engineering principles to the study

of biological systems

Equine Of or pertaining to a horse

Etiology A scientific account of the causes of a disease

Extension Increase in saggital plane angle between two

segments

External Negative rotation about the axis defined by the long

Rotation axis of the bone

Flexion Decrease in saggital plane angle between two

segments

in vitro Dealing with cadaver specimens

in vivo Dealing with live specimens

Kinematic The study of the motion of bodies

Lameness Abnormal locomotion resulting from an injury or

physiological defect

Lateral With respect to the limb, the side which faces away

from the body, perpendicular to a line between the

head and tail

Medial With respect to the limb, the side which faces towards

the centre of the body, perpendicular to a line between

the head and tail

Morphology The science of the forms and structures of organisms

Palmar In the digit, this refers to the rear facing side of the

digit

Proximal In the limb, the longitudinal direction towards the

body of the horse

Saggital A vertical plane through the animal parallel to the

median plane

Trotting A gait in which the forelimb and the diagonally

opposite hind limb move as a unit and in opposition to

the other diagonal pair

1. Introduction

1.1. Historical Perspective

Interest in equine locomotion dates as far back as the Shang dynasty (1750 – 1045 BC). In ancient China, the fundamental importance of the horse in war and agriculture necessitated the expansion of understanding and treatment of lameness in the equine limb (Chang, 1980). Similar interest appeared later in ancient Greece, where in 380 BC Xenophon authored his treatise *The Art of Horsemanship* (Xenophon, 380 BC). This and a similar study by Aristotle at approximately the same time on the equine locomotor system (Aristotle, 360 BC) remained the definitive works in the western world on the nature of human and horse interaction throughout the next two millennia.

The importance of the horse, and hence the importance of developing a fundamental understanding of the pathologies in the horse, cannot be understated. For centuries, beginning with the nomadic warriors in Mongolia and the Ukraine and proceeding to the highly effective cavalry of the late 19th century, there have been few sights more intimidating on the battlefield than the figure of a mounted warrior. During these years, the

numerous advances in the technology pertaining to the use of horses as instruments of war and agriculture revolutionized the military, economic, and political systems around the world.

The horse continued to play a significant role in both warfare and agriculture until early in the 20th century when its utility was eroded by the development of the internal combustion engine, resulting in a loss of military importance and the inevitable replacement of the horse in civilian use by automobiles and tractors. The loss of the practical need did not, however, negate the bond that had developed between man and horse over the previous centuries. The overall economic growth seen in the United States and western Europe through the years following the second world war has resulted in a resurgence of horse ownership for both equestrian sports and as companion animals. This is evidenced by the increased popularity of equestrian events such as the world equestrian games, the Rolex circuit, and the Olympic competitions.

This increase in ownership coincided with a renewal of interest in the study of equine sports science. This field, which had been actively pursued in Germany during the inter-war period by pioneers such as Wiechert (1927), Moskovits (1930), Kadletz (1937), and Kruger (1937, 1938), was left languishing in the post-war period in Germany as focus shifted from scientific pursuits to reconstruction (van Weeren, In Press). Slowly, however,

as economies recovered, horses ownership was once again feasible, and hence research into equine gait and gait pathologies was once again an area of active pursuit. The shift in horse usage from transportation and farm work to competitive sports required a more strenuous exercise schedule, which brought a need for a deeper understanding of equine locomotion. The focus was shifted from functionality to highly efficient performance (van Weeren, In Press) and treatment of injuries.

By far the most common equine injuries studied and treated in veterinary medicine are those of the locomotor apparatus (Rossdale et al, 1985), collectively referred to as lameness. Throughout the 1970s, 1980s, and 1990s, a substantial body of work has been accumulated that has fundamentally revolutionized the understanding of the equine locomotor apparatus and, hence, improved the effectiveness and quality of life of the sport horse. In spite of this, however, the understanding of equine locomotion remains limited, particularly as compared to the status of similar research into human locomotion.

1.2. Equine Biomechanics

In order to be an effective rider, it is necessary to have a fundamental understanding of the motion of the horse. Hence, studies of equine biomechanics can be tangentially seen in every study on effective horsemanship, from Xenophon (380 BC) to de Pluvinel (1626) to modern masters of equitation such Charles de Kunffy and Richard Shrake. As previously stated, however, scientific studies have been far less numerous and were limited by the available technology until the advent of computerized data collection and modeling methods. These tools have dramatically increased both the quantity and quality of data available to researchers in the general biomechanics community as well as that dedicated to the study of equine locomotion.

Some research has been performed in the area of animal gait analysis using techniques practiced in human medicine. Equine and canine locomotion have been regularly studied in order to improve athletic performance and to improve understanding of the causes, symptoms, and treatment of lameness.

Gait analysis typically involves the measurement of temporal, linear, and angular kinematics, ground reaction forces, joint moments, and/or joint powers. Through the observation of these parameters, normal gaits can be

characterized and pathologies can be detected earlier and treated more effectively (Whittle, 1991).

1.3. Computer Models in Biomechanics

The use of computer models revolutionized the study of locomotion.

Beginning in 1969 with the first two-dimensional analysis of the human arm (Chaffin, 1969), to recent advances in surgical techniques utilizing computer models to prepare for difficult procedures (McGurk et al, 1997), computer models have allowed the study of the interactions of complex bones, muscles, and soft tissue. These studies have resulted in improved artificial joints, advancements in clinical diagnosis of musculo-skeletal disease, and a better comprehension of the mechanical interactions within joints.

The primary focus of much of the work performed in human anatomy is the creation of accurate models of joints. These models, generally of a single joint such as the hip (Tsumura et al, 1998) or knee (Sathasivam and Walker, 1997), or occasionally of more complex areas such as the hand (Buford and Thompson, 1987; Van Sint Jan et al, 1997), or ankle (Delp et al, 1990), are able to demonstrate the natural motion of the bones within the joint as well as to provide a basis for more accurate dynamic simulations and analyses. In spite of the importance and significance of many of these human studies, cost

and technical challenges have limited the use of these techniques in the study of animal locomotion.

A few notable examples of research utilizing computer models to study the structure and function of the equine locomotor apparatus should be mentioned. These include comprehensive dynamic models (van den Bogert et al, 1989), limb specific models pertaining to kinematics and joint moments and powers (Colborne et al, 1998; Lanovaz et al, 1999), and models focusing on the dynamic or static loading and response of specific segments such as the sesamoid bones of the metacarpophalangeal joint (Cheung and Thompson 1994), metacarpus (Les, et al 1997), and hoof (Hogan 1991). These models have proven invaluable in the general understanding of the nature of equine locomotion and the process of adaptive development of the equine skeletal structure.

Although these studies remain the most comprehensive research performed in this field to date, a great deal of work remains to be done in the development of accurate and specific joint models, particularly in regions of high degrees of complexity. In humans, analysis has been performed to create gross models of gait, and specialized models have been developed to analyze the interactions of particular joints. Special emphasis has been placed on the human hip and knee due to the overall importance of quantifying the effect of medical procedures involving the replacement of

these joints. Interest in horses, however, typically focuses on the stifle, carpus, tarsus, and fetlock, due to the high incidence of lameness originating at these joints.

1.4. Research Objectives

The focus of this research is to develop a method of creating an accurate and comprehensive model of the equine tarsal joint and to validate the model for its accuracy and utility. This research, in addition to its benefits as a tool for understanding the complexities of equine locomotion, has the potential of being extended into a more comprehensive model of the tarsus that will include information on the dynamic loading throughout the gait. The final goal is to develop a sufficiently accurate computer model so as to provide a basis for future studies that would allow for improved clinical procedures in cases pertaining to tarsal joint injuries, and limit the necessity of using live subjects in the study of tarsal joint mechanics.

2. Anatomy of the Equine Hindlimb

2.1. Structure and Morphology

The horse is by its nature a cursorial (running) species. The survival of the animal was innately dependent on its ability to outrun predators. Because of this, the evolution of its locomotor apparatus was towards speed and economy of movement (Figure 1).

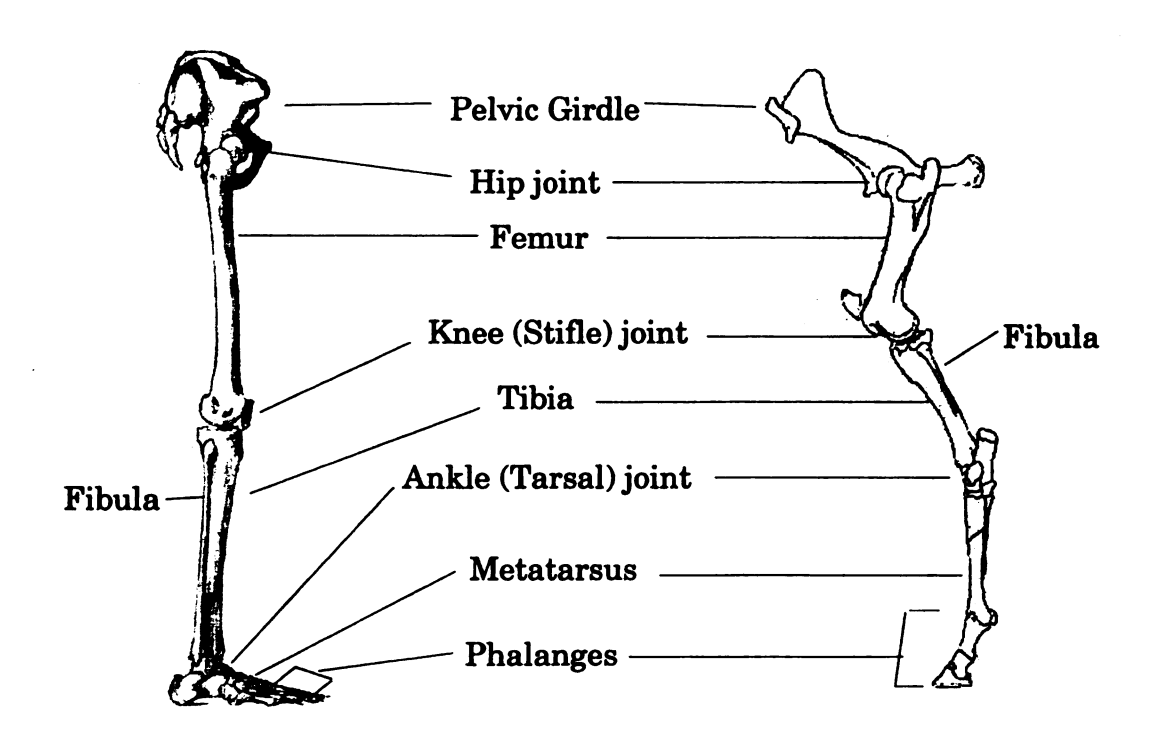


Figure 1. Comparison of anatomy between the human leg and equine hindlimb (equine specific names in parenthases)

To achieve optimal efficiency, the limbs of the horse have adapted for planar motion. The bones at joints interlock tightly and are constrained by collateral ligaments to prevent out-of-plane motion. Additionally, the fibula and tibia have fused; and only a single functional digit exists, both of which serve to prevent rotation of the distal limb.

In order to increase the efficiency of gait, the heavy muscle mass is confined to the proximal limb. Joints distal to the tarsus are controlled by long tendons that cross the tarsus and attach to muscles in the proximal limb. This results in an overall shifting of the mass moment of inertia closer to the body, allowing for much faster motion of the limbs than would be possible with additional mass in the distal segments.

The metatarsus and phalanges are elongated, and elevate the tarsus from the ground. The horse moves in an unguligrade stance, which is to say that it walks on the tips of the phalanges (like a ballerina "on point"). This serves to increase the effective limb length, hence increasing the overall stride length and subsequently the top speed of the animal. This is as opposed to human stance, referred to as plantigrade, with the metatarsals and phalanges parallel to ground during weight bearing, or the digitigrade canine stance, in which the phalanges are parallel to the ground but the metatarsals are elevated.

2.2. Anatomy, Motion, and Pathology of the Tarsal Joint

2.2.1. Bones of the Tarsal Joint

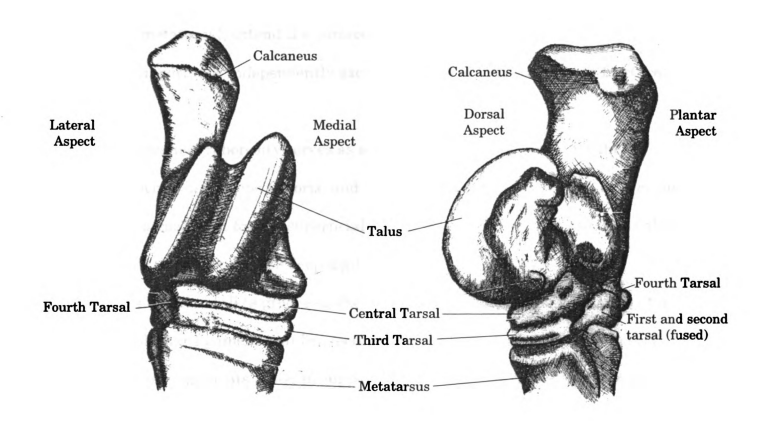


Figure 2. Right tarsal joint,

Figure 3. Right tarsal joint, medial view

The tarsus is a composite joint located distal to the tibia and proximal to the metatarsus (Figures 2 and 3). The joint capsule itself contains all or parts of the tibia; calcaneus; talus; central tarsal; the first through fourth tarsal bones; and the second, third, and fourth metatarsal bones.

It is worthwhile to note here the unique morphology of a few of these bones; the first and second tarsal bones are fused at birth and, hence, move collectively as a single unit. The second and fourth metatarsals are, in fact, vestigial remnants of 'digits'. These bones, attached via ligaments to the third metatarsal, extend the surface area of the third metatarsal and are of little importance independently except for cases of inflammation or fracture.

The calcaneal tuberosity serves as a lever arm for the insertion for the gastrocnemius, biceps femoris, and semitendinous muscles, as well as serving as an attachment for the superficial digital flexor tendon. The calcaneus also affords protection for the deep digital flexor tendon as it runs over the sustentaculum tali (a groove on the talus). The calcaneus is stabilized by the long plantar ligament that connects to the metatarsus on its plantar aspect. Accessory ligaments assist in supporting the joint. These ligaments originate on the talus and calcaneus and insert primarily onto the metatarsals.

2.2.2. Intertarsal Joints

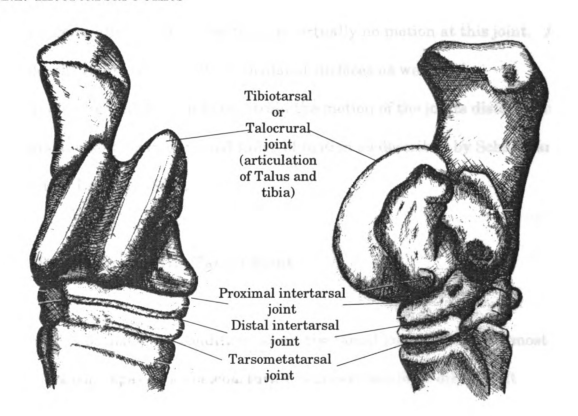


Figure 4. Right tarsal joint,

Figure 5. Right tarsal joint, medial view

The tibia interfaces with the talus via the tibiotarsal or talocrural joint, constrained by the talar trochlea (ridges) that define the rotation of the joint. A majority of the motion at the tarsal joint as a whole occurs at the tibiotarsal articulation (Schamhardt et al, 1984; Badoux, 1987), and occurs in the sagittal plane, though all horses show a degree of out of plane tarsal motion due to the oblique orientation of the trochlea of the talus. The proximal and distal intertarsal joints allow some degree of sliding motion, but are constrained by collateral ligaments around the tarsus. Similarly, the

motion of the tarsometatarsal joint is restricted by the collateral ligaments, and it is generally accepted that there is virtually no motion at this joint. As a whole, the complexities of the articulated surfaces as well as the surrounding ligaments greatly constrain the motion of the joints distal to the tibiotarsal, resulting in a limited range of motion as described by Schamhardt (1984) and Badoux (1987).

2.2.3. Pathologies of the Tarsal Joint

A number of pathological conditions affect the tarsal joint. One of the most common is bone spavin, an osteoarthritic degenerative joint disease. It typically affects the medial aspect of the distal intertarsal and tarsometatarsal joints (Adams, 1977). This condition results in pain during flexion of the tarsus, which results in a reduced flight arc and a shortening of the stride (Adams, 1977). Treatment of this condition typically involves anti-inflammatory medication, sometimes in combination with corrective shoeing or, in more serious cases, surgical intervention to denervate or fuse the affected joints. In spite of these treatments, more than half of the horses diagnosed with spavin do not respond and remain chronically lame (Adams, 1977).

Additional pathologies related to tarsal joint lameness include tendon and ligament inflammation induced by injury or abnormal abrasion due to poor

conformation. One of the most common is curb, in which the plantar ligament that stabilizes the calcaneus becomes inflamed (Adams, 1977).

Although mild cases are easily treated with anti-inflammatories (administered orally, topically or by injection), cases due to poor conformation tend to recur and become chronic.

These and other pathologies of the tarsal joint remain difficult to treat due to the complexity of the joint. Additional understanding of the kinematics of normal and pathological locomotion could substantially improve our understanding of the etiology, diagnosis, and treatment of tarsal joint lameness.

3. Method of Investigation

3.1. Collection and Preparation of Articulated Specimen of the Tarsal Joint

The specimen used in the development of the computer model was harvested from a six-year-old thoroughbred euthanized by the Michigan State

University College of Veterinary Medicine, Department of Large Animal

Clinical Sciences. The subject was euthanized for reasons unrelated to locomotion. The specimen was harvested by transecting the hindlimb through the middle of the tibia, and also transecting the middle of the metatarsus. This was performed within 30 minutes of euthanasia, and the specimen was subsequently frozen until the data were collected.

3.2. Computerized Tomography Scan of Articulated Tarsal Joint

The first step in the development of the kinematic model of the joint was the creation of accurate computer models of the bones comprising the joint.

Computerized tomography (CT) scans were taken of the fully articulated

joint. The scans were taken on a General Electric 9800 CT machine (General Electric Medical Systems, Waukesha, WI) at 120 kV and 120 mA. The small field of view was selected, resulting in a pixel to millimeter ratio of 2.048. Scans were taken at 3 millimeter increments with an exposure time of 2 seconds. The scan data were recorded to 10.5" reel tape, which was subsequently downloaded to a Sun UltraSparc 1 workstation (Sun Microsystems, Palo Alto, CA).

3.3. Preparation of Disarticulated Tarsal Bones

After scanning the fully articulated joint, it was disarticulated. The initial separation was performed using standard dissection techniques to isolate the bones and remove the collateral ligaments which support the joint. In order to separate the central tarsal and third tarsal bones, which have a large amount of connective tissue deep within the joint capsule, as well as to remove the remaining connective tissue, the joint was placed in a skeletal preparation box containing dermestid beetles (genus *Dermestes*), which are commonly used in the preparation of anatomical specimens as they consume soft tissue without degenerating the bone.

To restrict the motion of the loose bones during the process of CT scanning, they were embedded in silicone in a cylindrical container. Previous research indicated that the x-ray diffusion of a non-metallic substrate silicone was

sufficiently different from that of bone as to allow clear differentiation of the two (Ocello and Rosenstein, unpublished data). After pouring the silicone around the separated tarsal bones, the container was placed in a vacuum to degassify for a period of 30 minutes, then left to cure at room temperature and ambient pressure for two days.

In order to reconstruct the three-dimensional structure of the bones following scanning, it was necessary to provide a fixed set of points that were visible in all scans that would indicate the three-dimensional position of the bones. An additional concern in the construction of this reference frame was that metallic substances could not be used, as they have high levels of x-ray absorptivity which degrades the quality of the CT scan.

The final design for the coordinate axis definition consisted of two nylon wires, 0.4 mm in diameter, stretched taught above the bone and silicone. The wires were attached via angle brackets to a wood frame with an angle of approximately 90 degrees between them. The silicone/bone matrix container was then secured to the wood frame by epoxy resin.



Figure 6. Final design of coordinate apparatus

3.4. Computerized Tomography Scan of Disarticulated Tarsal Bones

CT scans were subsequently taken of the container containing the tarsal bones embedded in silicone. This assembly was scanned along two axes approximately 90 degrees from each other. This was necessary due to the limits on resolution of CT scans. Each scan consists of a cross-sectional image of the scan region. This results in a high resolution image in the scan plane, but along the axis of the scan the sequence of images are of much lower resolution. By conducting two separate scans separated by a 90-degree rotation, there is high resolution image data in three-dimensions.

A sequence of 150 scans was taken using the same CT machine and parameters as used for the articulated scans, however these scans were taken at 1.5 mm increments to ensure a high degree of accuracy for the models.

3.5. Image Processing

Data from CT scans are stored in a proprietary format specific to the model and manufacturer of the machine. This is primarily legacy code due to the use of CT scans prior to the development of imaging standards but is also necessary to some degree due to the quantity of data present for each image. The GE 9800 format consists of a 24-bit, grayscale imagemap of the 512 x 512 image. In order to use these images for any purpose other than viewing on the GE 9800 CT console, they must be converted to a more commonly available image format.

An open source initiative in the medical community has fortunately resulted in the distribution of a toolkit for this purpose (American College of Radiology, 1993). This set of programs, referred to as the DICOM toolkit, can be used to convert the proprietary image format of CT (as well as MRI and PET) manufacturers into the more accessible Portable Graymap (or PGM) format. In order to improve the specific resolution for bone, however, it was necessary to slightly modify the code of the DICOM toolkit such that the

grayscale values associated with bone were enhanced and those associated with the silicone embedding material were reduced.

A batch processing script was developed to convert the GE 9800 format CT scans into bitmaps en masse. This script utilized public domain code from the DICOM toolkit to convert the image to a portable graymap (PGM) format, and subsequently to a bitmap format.

At this point, the data consisted of two sets of 150 independent sequential bitmap grayscale images. The exact three-dimensional point locations of the bone edges were determined by application of an edge detection algorithm to the images. For this purpose, a program was written in MATLAB (Mathworks, Inc., Natick, MA) that took a user defined region of the image and analyzed it using edge detection algorithms.

3.6. Edge Detection Algorithm

All edge detection algorithms operate on similar principles, that of seeking maxima in the derivative or gradient of the given image. Specific techniques vary however in how this principle is applied. The Sobel (Jahne, 1997) and Roberts (Jahne, 1997) methods rely on fixed vector differentiation from the original image. The result of this is that the gradient is accurately calculated only in a single direction, and the edge data normal to the selected vector are

lost. Although each of these methods use slightly different techniques (Roberts using a simple finite difference technique, and Sobel using a weighted average technique), without a priori knowledge of the pertinent gradients and rotation of the image to align them appropriately to the direction of gradient calculation, they will not perform well. In the case of the images being analyzed here, the variability in edge direction effectively rules out these techniques.

The Canny edge detection technique as described by Canny (1984) and Schunck (1986) improves on previous algorithms by employing a gaussian filter to reduce image noise. A two-dimensional gaussian function is used to filter the image prior to analyzing the gradient (Equation 1).

$$g(x,y) = e^{\frac{-(x^2+y^2)}{2\sigma^2}}$$
 (1)

This function effectively acts as a low pass filter with a definable gaussian parameter, σ , that allows for control over the degree of smoothing performed prior to determining the gradient.

Once the image has been smoothed, the gradient is then calculated using the partial derivative of the filter in both the x and y directions, and subsequently adding the results (Equations 2 and 3).

$$\frac{\delta}{\delta x} \approx \frac{F(x_{i+1}, y_j) - F(x_i, y_j) + F(x_{i+1}, y_{j+1}) - F(x_i, y_{j+1})}{2}$$
(2)

$$\frac{\delta}{\delta y} \approx \frac{F(x_i, y_j) - F(x_i, y_{j-1}) + F(x_{i+1}, y_j) - F(x_{i+1}, y_{j-1})}{2}$$
(3)

The magnitude and direction of the gradient were subsequently solved by a simple magnitude and angle solution as shown by Schnuck (1986) (Equation 4).

$$\rho(x_i, y_j) = \sqrt{\left[\frac{\delta}{\delta x}(x_i, y_j)\right]^2 + \left[\frac{\delta}{\delta y}(x_i, y_j)\right]^2}$$
 (4)

By defining the threshold value, the allowable minimum gradient magnitude for defining an edge could be controlled. A sample image demonstrating the Canny edge detection algorithm is shown figures 7 and 8.

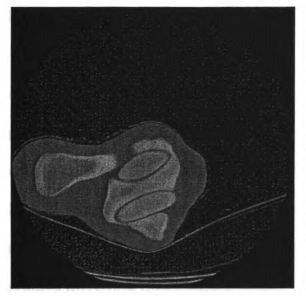


Figure 7. Cross sectional image of the tarsus transecting the calcaneus and tibiotarsal joint



Figure 8. Cross sectional of image after applying the Canny edge detection algorithm (Schnuck, 1986)

Typically, one performs edge thinning and edge connection analysis on the image after performing the edge detection; however, the results of the edge detection alone were found to be sufficient for accurate modeling of the bones.

When the bone surface does not lie perpendicular to the plane of the scan, the edge of the bone appears as a region with a variation of grayscales, none of which is sufficiently distinct to produce a well defined edge by a differential gradient method. Consequently, a threshold cutoff was used on these areas prior to the gradient analysis in order to improve the edge definition. The threshold was chosen based on user input and could be modified to improve the edge quality of a specific image.

3.7. Creation of the Solid Model

After performing the edge detection in MATLAB, the global coordinates of points representing the edges of the bones were written to a file in the format used by the batch scripting method of the I-DEAS solid modeling package (SDRC, Milford, Ohio). The I-DEAS package was selected due to availability and the capabilities of the software for medical reconstruction. Previous studies including finite element analysis of the human skull (Remmler, 1998) and equine metacarpus (Chung and Thompson, 1993) indicated that it would be satisfactory not only for this project but for subsequent research into dynamic loading and simulations.

After the output files from the MATLAB program had been read into I-DEAS, the result was a 'point cloud' representing the outside surface of each bone as seen by the two orthogonal scan axes. These independent data sets were oriented with respect to each other by determining the angle of rotation and translational position of the relative scans based on the reference coordinate frame defined by the nylon lines on the scan frame. The values were determined by digitizing the coordinates of the lines in the sequential CT scan images and conducting a linear regression of the datapoints to recreate the vectors defined by the nylon lines.

After the (relative) point clouds had been aligned in three-dimensions, solid models were created from these points. Three separate methods were employed to create the models: lofting, curve mesh, and surface stitching.

Lofting is a process by which surfaces are created from a sequential set of cross sectional curves. It is used in computer aided-design and modeling packages for the creation of highly sculpted surfaces with small variations in curvature, but it performs poorly in regions in which the model has a substantial variation in curvature or creates a sharp angle with adjoining surfaces. It uses polynomial interpolation between sequential complete curves (i.e. curves whose endpoint is coincident with the start point). This method is highly suitable for the creation of models of bones along their primary axes.

In order to use this method, it was necessary to create a single continuous curve in a single plane representing the outside perimeter of the bone being modeled. The I-DEAS software package uses non-uniform rational basis splines (NURBS) to create curves through given points.

NURBS are frequently used in computer applications for drafting, engineering design, or drawing. They are extremely powerful in that they allow for the definition of 'smooth' surfaces (those without sharp bends) with a relatively small amount of data. A NURBS is mathematically defined by a

set of geometrical locations called control points. These control points define the curve using the weighted local average of their relative locations (the weighting being based on user defined parameters of the dominance of a particular point in the curve definition). Hence each control point in theory affects all parts of the curve, with the closest points having substantially greater impact than those farther away. By using the three-dimensional locations of the bone edges derived from the CT scans as the control points, and heavily weighting them to force the curve to trace the path, an accurate representation of the bone surfaces was defined. After these continuous curves had been created, solid models were developed using the lofting procedure to describe the surfaces defining the primary axes of the bones (Figures 9 and 10).



Figure 9. Cross section curves used for loft definition on the metatarsus



Figure 10. Resultant surface from the lofting technique on the metatarsus

Since the lofting process performs poorly in areas with high degrees of variability in curvature, it was unsuitable for the majority of the contact surfaces of the bones. For those surfaces, either curve meshing or surface stitching was used.

Curve meshes use a grid of intersecting curves to create the surface representation. The intersecting curves are produced using NURBS, similar to the technique described for lofting. The highly sculpted surfaces of the contact areas of bones make the curve mesh ideal for most of these areas.

For each surface, a series of non-continuous curves were created describing the cross section of the surface in a series of parallel planes called 'profile curves'. The separation of the curves, typically 1.5 or 3 mm, was dependent upon the complexity of the surface with more curves being needed to describe more complex surfaces. A second set of curves, referred to as 'rail curves', were used to define the connection of the profile curves on their edges, and give additional information on the contours across the surface. The software then interpolated these curves to create the surface definition (Figures 11 and 12).

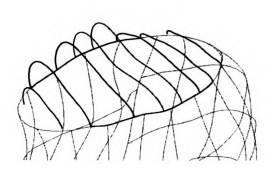


Figure 11. Cross section and rail curves used for surface definition on the calcaneus



Figure 12. Resultant surface from the mesh of curves technique on the calcaneus

For the metatarsus, however, the proximal surface, which is in contact with the third and fourth tarsal bones, was too complex even for this technique due to the concavity at the point of contact between the fourth tarsal bone, the third tarsal bone, and the metatarsus. The inability for the software to accurately interpolate the surface definition in these regions necessitated the use of surface stitching. This method uses low weighted control point NURBS to interpolate a cubic spline between three control points to create a grid of roughly square surface sections, which were subsequently combined or 'stitched' at the edges. This method, although lengthy and tedious, results in highly accurate surface representations due to the fact that it is a combination of 1-1.5 mm squares developed directly from the CT scan data, rather than from interpolated surface information (Figures 13 and 14).

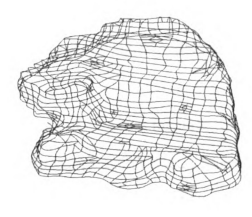


Figure 13. Curve grid used for surface definition on proximal surface of the metatarsus



Figure 14. Resultant surface from the surface stitching technique on the metatarsus

3.8. Development of Tool for Model Visualization

Once the computer representations had been constructed, the next step of the process was to develop a method of linking the models with spreadsheet data derived from external kinematic measurements. This was important due to the interest in using the models as visualization tools for the three-dimensional kinematics of the joint and as a research tool to study the range of motion between the joints in relation to the effects of degenerative diseases in the tarsus. It is possible to perform simple animation based on external tab delimited data in I-DEAS, the modeling package used to develop the solid models; but the flexibility of application intended in the original concept of the project required more powerful animation and rendering software. The use of a proprietary file format by SDRC in the I-DEAS product precluded direct use of the solid model data in I-DEAS.

A number of external formats were considered, including Virtual Reality
Markup Language (VRML), Microsoft DirectX, Stereolithogrophy (STL)
definition files, and Initial Graphics Exchange Standard (IGES). An
evaluation of the respective accuracy of the formats indicated that IGES did
not reliably produce models of sufficient surface accuracy for the purposes of
this study. The VRML format appeared ideal initially, but was subsequently
found to have a number of drawbacks relating to code limitations for collision
detection and file size limitations in VRML viewers. Although the STL
format performed reasonably well, it was determined to use the DirectX
format due to the publicly available resources for rendering and animation.

DirectX retained mode relies upon binary encoded object data for the creation of models, so it was necessary to convert the text based VRML format to that used by DirectX. A Visual Basic program was written to perform this conversion. Once the binary formatted DirectX files had been created, they were imported into a second program, which allowed the user to define the specific relations between geometric models and kinematic data. This program used the input data to animate the models, allowing the animation to be viewed from any position or angle (Figure 15).

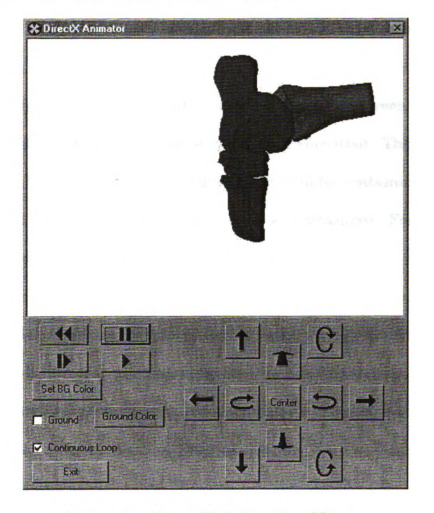


Figure 15. DirectX Animation Viewer

3.9. Model Validation by Volumetric Measurements

The objective of this research was to develop a highly accurate model of the bones of the equine tarsal joint. In order to validate the quality of the models a comparison was made between the volumes of the original bones and their respective computer models. The volumetric measurement was performed by observing the volume of displaced fluid when the specimen was placed in a container of liquid. Due to the natural porosity of bone, the specimens were sealed with a thin layer of petroleum jelly to prevent absorption of the liquid.

Due to the large difference in apparent relative volumes between the largest and smallest bones, two displacement techniques were used. The first and second tarsal bones were placed in a graduated cylinder containing the measurement fluid, and the increased volume was measured. For this technique, water was a satisfactory fluid.

Cylinders wide enough to accommodate the larger bones of the tarsal joint have a large surface area and this decreases the sensitivity of the technique. Therefore, instead of performing a direct volumetric measurement of the larger bones, an indirect measurement based on the mass and density of the displaced fluid was used.

A nonionic wetting agent and detergent was added to water to reduce its surface tension. The mass of known volumes of this fluid was measured five times using an electronic rate calculating balance (Pelouze, Chicago, IL) and the resulting calculated densities were averaged to reduce the effect of erroneous measurements. Approximately 1 litre of fluid was placed in a large cylinder that had a hole and spout near the top. Any change in the height of the liquid would result in an overflow through the spout into a beaker. Each bone was slowly lowered into the water and the overflowing liquid was collected and weighed. The volume of the bone was calculated from the experimentally determined density of the displaced fluid. For each of the tarsal bones, the volume measured by one of the displacement techniques was compared with the volumes calculated by the I-DEAS software package.

3.10. Application of Model

In order to indicate the practical research aspects of the model, a pilot study was conducted to evaluate the hypothetical motion of the tarsal joint as projected by the computer model with experimentally measured kinematic motion. According to the cadaver study performed by Schamhardt et al (1984), almost all motion observable using in vivo techniques should occur at the tibiotarsal joint. The model was used to validate this assumption by observing the correlation between flexion and extension of the tarsal joint

and the abduction/adduction and internal/external rotation of the joint (Figure 16).

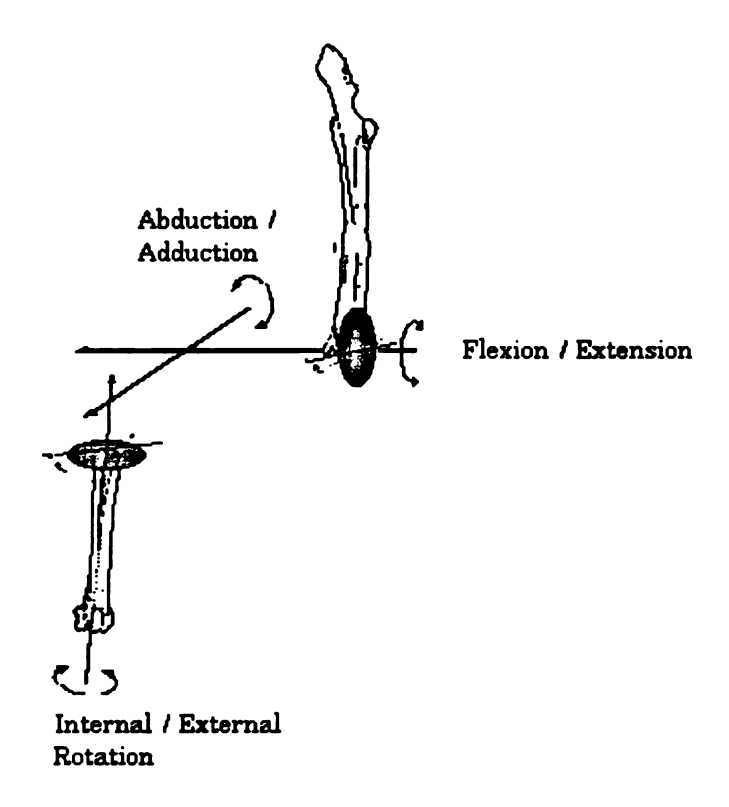


Figure 16. Rotational axis definitions used in analysis of joint angles

The motions of the tibia and metatarsus were recorded by the placement of reflective markers on the skin overlaying palpable bony landmarks (Soutas-Little, 1996, Lanovaz et al., Submitted). Marker locations were chosen that had minimal skin displacement during locomotion and such that an axis vector was established along the lateral side of the diaphysis of the bone, and a second vector was oriented in the mediolateral direction at the joint (Figures 17 and 18).

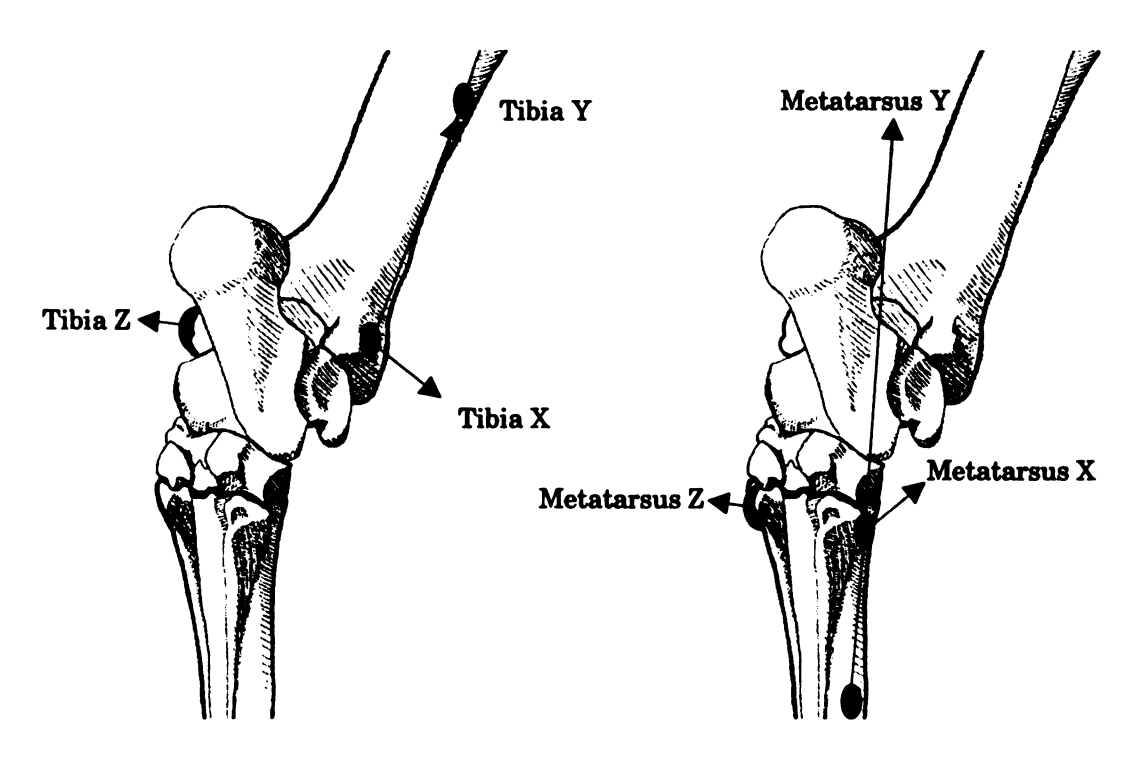


Figure 17. Marker locations used on the tibia for kinematic data collection

Figure 18. Marker locations used on the metatarsus for kinematic data collection

An 11 year old Thoroughbred of approximately the same size and weight as the horse used for the computer model of the tarsal joint was filmed using two Panasonic AG 450 video cameras (Matsushita Electric Corp., Secaucus, NJ) while moving on a Mustang equine treadmill (Kagra, A.G., Fahrwangen, Switzerland) (Figure 19).

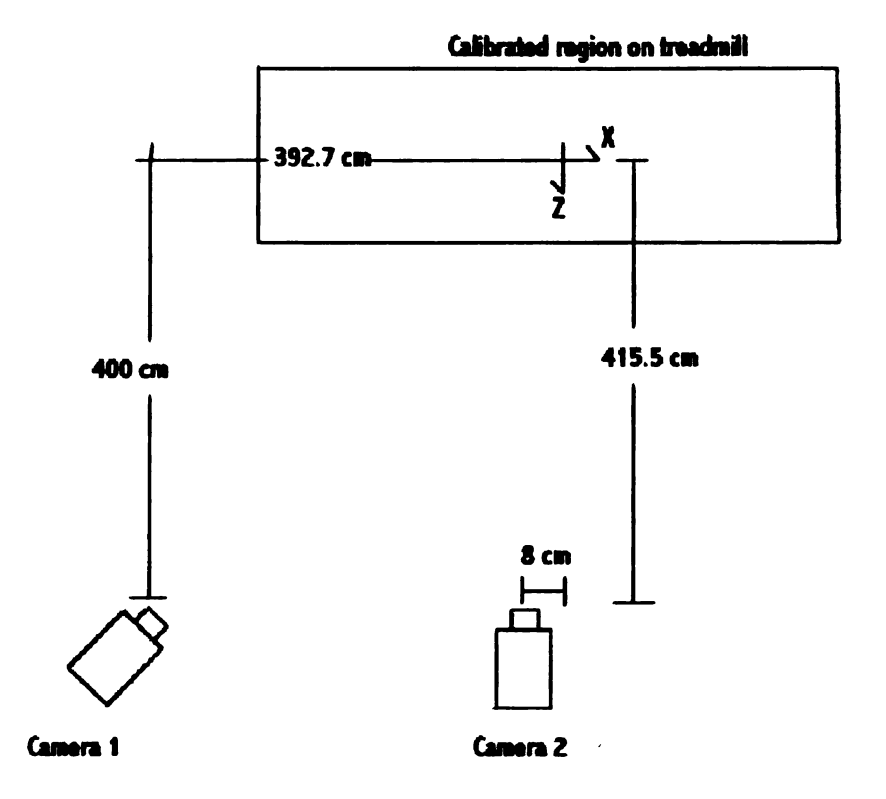


Figure 19. Experimental Setup for Kinematic Data Collection

The horse had been previously trained on the treadmill and its motion was typical for a healthy horse moving at the studied gaits. Recordings were made of the horse trotting at 4.2 m/s.

The resulting kinematic data was analyzed using the Ariel Performance

Analysis System (Ariel Dynamics, Trabuco Canyon, California). The results
of this analysis described the three-dimensional translation and rotation of
the tibia and metatarsus in the segmental coordinate system.

The resulting experimental data were then compared to the model based motion of the tarsal joint based on the assumption that all motion occurred at the talocrural joint. This projected motion was determined from the computer model of the talus. The curvature of the talus at its articulation with the tibia was analyzed to derive the estimated three-dimensional path curve for the tarsus for a given flexion angle.

In order to determine the model based three-dimensional location and orientation of the tibia, the curvature of the talar trochlea was determined using the minima of the groove on the talus along which the tibia moves. This curve was found by intersecting a plane with the computer model of the talus and taking the minimum point on the resulting curve.

The three-dimensional points were used to define the curve of the groove between the talar trochlea, and hence define the motion of the tibia (Figure 20).

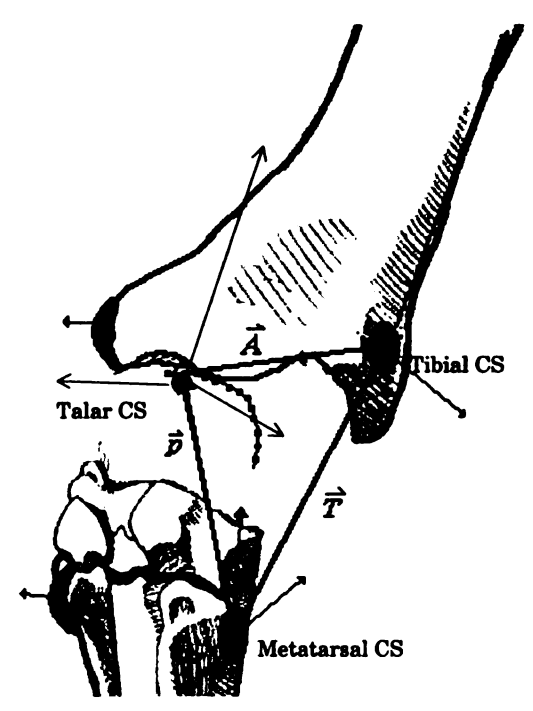


Figure 20. Metatarsal, talar, and tibial coordinate system definitions for model based analysis

Using a global coordinate system coincident with the kinematic metatarsal coordinate system, the talar X vector at a point p was determined using an approximation of the instantaneous tangency calculated as shown in equation 5.

$$\vec{X}_{\text{talus},p} = \vec{p}_{n+1} - \vec{p}_{n-1} \tag{5}$$

where

 \vec{p}_n is the vector from the global coordinate system to the *n*th three-dimensional point defining the groove between the talar trochlea.

The talar Z vector was found by determining the normal of the instantaneous plane formed by three successive points defining the talar trochlear groove (Equation 6).

$$\vec{Z}_{\text{labus},p} = (\vec{p_n} - \vec{p_{n,l}}) \times (\vec{p_n} - \vec{p_{n,l}})$$
(6)

The final coordinate vector for the tibia was found by taking the cross product of the instantaneous talar X and Z vectors (Equation 7).

$$\vec{Y}_{talus,n} = \vec{Z}_{talus,n} \times \vec{X}_{talus,n}$$
 (7)

The unit vectors defining these coordinate axes (Equations 8-10) were used to create the transformation matrix between the metatarsal coordinate system and the instantaneous talar coordinate system (Equation 11).

$$\hat{i} = \lambda_{x,X} \hat{I} + \lambda_{x,Y} \hat{J} + \lambda_{x,Z} \hat{K}$$
(8)

$$\hat{j} = \lambda_{y,x} \hat{I} + \lambda_{y,y} \hat{J} + \lambda_{y,z} \hat{K}$$
(9)

$$\hat{k} = \lambda_{, x} \hat{I} + \lambda_{, y} \hat{J} + \lambda_{, z} \hat{K}$$
 (10)

$$[R] = \begin{bmatrix} \lambda_{x,X} & \lambda_{x,Y} & \lambda_{x,Z} \\ \lambda_{y,X} & \lambda_{y,Y} & \lambda_{y,Z} \\ \lambda_{z,X} & \lambda_{z,Y} & \lambda_{z,Z} \end{bmatrix}$$
(11)

A vector A relating the each of the tibial coordinate system points to the talar point was defined using the grounded coordinate system, and this vector was transformed into the tibial coordinate system using the rotation matrix (Equation 12).

$$\vec{a} = [R]\vec{A} \tag{12}$$

This vector and the rotation matrix R were used to resolve the location of each of the tibial markers in terms of the grounded coordinate system (Equation 13).

$$\vec{T} = \vec{p} + [R]^{\mathsf{T}} \vec{a} \tag{13}$$

where

 \overrightarrow{T} is the resultant vector from the metatarsal coordinate system

to the tibial coordinate system marker and

 $ec{p}$ is the vector from the metatarsal coordinate system to the talar point location.

This calculation was performed for each talar point location corresponding to 0 to 180 degrees of tibiotarsal flexion using a program written in MATLAB, and the tibial positions and orientations were compared to the results of the kinematic analysis.

4. Results

4.1. Computer Models of the Bones of the Tarsal Joint

The focus of this research was the development of a comprehensive and accurate model of the bones and joints of the equine tarsal joint. Since this was the primary goal, the results of the research were the computer models themselves, and most of the research consisted of the development of the modeling technique to ensure accuracy and repeatability in the process.

The relative complexity of each model may be evaluated qualitatively by examination of the total number of cross sectional curves and surfaces required to construct the model (Table 1).

Table 1. Number of cross sectional curves and surfaces in computer

model of each bone				
Bone	Number of cross section curves	Number of surfaces		
Tibia	134	27		
Talus	112	28		
Calcaneus	126	36		
Central Tarsal	66	14		
First and second tarsal	41	29		
Third tarsal	59	46		
Fourth tarsal	52	29		
Metatarsus	98	889		

4.1.1. Tibia



Figure 21. Distal end of tibia



Figure 22. Computer model of distal tibia

The complexity of the distal surface of the tibia which contacts the talus, and the need for a high degree of accuracy at this location due to the interest in the motion at the junction of the tibia and talus, required that special emphasis be placed on the data obtained for this surface. By examining the

two point clouds and judiciously using the points from the image processing of the two scans, the surface was created with a high degree of accuracy, which is evident both by a visual comparison of the computer model to the bone (Figures 21 and 22), and by comparison of the surface to surface contact at the talocrural joint throughout its range of motion.

4.1.2. Talus



Figure 23. Talus specimen



Figure 24. Computer model of talus

An exceptional degree of accuracy was demanded in the model of the talus, for the same reasons as specified for the tibia. Additional challenges were posed by the fact that this bone made surface to surface contact with a total of five bones (tibia, calcaneus, central tarsal, first and second tarsal, and fourth tarsal bones). Surface interaction analysis via the interference analysis tools in I-DEAS indicated that the surfaces coincided very well

between the models. As each model was developed independently, this was assumed to indicate a high degree of accuracy in the models themselves (Figures 23 and 24).

4.1.3. Calcaneus



Figure 25. Calcaneus specimen



Figure 26. Computer model of calcaneus

The calcaneus acts as a lever arm and as a support surface for the tendons transferring forces to the segments of the distal limb. As such, it is necessary that the surface tolerance between it and the talus be extremely tight to

ensure stability and optimal transfer of the force through the tarsal joint. A comparison of the respective surfaces between the calcaneus and talus indicated that the model would lock the calcaneus in place accurately and prevent rotation, in the same way as seen in the joint itself (Figures 25 and 26).

4.1.4. Central and Third Tarsal Bones



Figure 27. Central tarsal bone specimen



Figure 28. Computer model of central tarsal bone





Figure 29. Third tarsal bone specimen

Figure 30. Computer model of third tarsal bone

The structures of the central and third tarsal bones are quite similar. They are both roughly elliptical bones that lock tightly to each other, supported by connective tissue deep within the joint. The surfaces of these bones presented excellent opportunities to evaluate the modeling process, as they should be smooth and have very similar reciprocating curvatures (Figures 27-30). The bone surfaces interface tightly, both with each other and with the surrounding structures (talus, metatarsus, first and second tarsal bone, and fourth tarsal bone). The computer models, however, fail to represent the roughness on the dorsal aspect of the interfacing surfaces to a high degree of accuracy, due to the limitations of resolution in the CT image data.

4.1.5. First and Second Tarsal Bone and Fourth Tarsal Bone





Figure 31. First and second tarsal bone specimen

Figure 32. Computer model of first and second tarsal bone





Figure 33. Fourth bone specimen

Figure 34. Computer model of fourth tarsal bone

Examination of the models of these bones indicate that they satisfactorily represent the general shape and areas of surface to surface contact (Figures

31-34). However, it is also evident that some of the surface intricacies have been lost in the modeling process due to their sizes with respect to the CT image resolution.

4.1.6. Metatarsus



Figure 35. Proximal end of metatarsus specimen

Figure 36. Computer model of proximal metatarsus

The proximal surface of the metatarsus is by far the most geometrically intricate and complex of the bones of the tarsal joint due to the discontinuity between the contact with the third tarsal bone cranially and, the first and second and fourth tarsal bones caudally. The surface stitching technique however resulted in an accurate representation of the surface when compared both visually with the original model (Figures 35 and 36), and by use of the interference checking techniques for the bone surface interaction.

4.2. Results of Volumetric Measurements

Few methods are available for validation of the geometry of the computer models, due to the fact that the best geometric data, derived from the CT scans, were used in the development of the model. By comparing gross volumetric differences between the computer model and the bone models, some indication of general accuracy may be determined (Table 2).

Table 2. Comparison of specimen volumes and calculated volumes of computer models

Specimen	Experimental Volume from specimen (cm²)	Theoretical volume from computer model (cm²)	Percent Difference
Tibia	214.33	201.81	5.8
Calcaneus	158.66	164.29	3.5
Metatarsus	136.39	144.15	5.7
Talus	172.58	166.19	3.7
First and second tarsal bone	7.93	7.58	4.4
Fourth tarsal bone	34.87	35.92	3.0
Central tarsal bone	27.90	28.38	1.7
Third tarsal bone	27.00	27.92	3.4

The volumes of all models correlated reasonably well with the measured volumes of the original bones, with the tibia and metatarsus having higher discrepancies than the other bones of the model.

4.3. Application of Model to Prediction of Motion of the Tarsal Joint

The assumption for the model prediction was that all observable kinematic motion occurred at the tibiotarsal joint and only along the path defined by the talar ridges. Regression equations correlating flexion/extension with internal/external rotation and abduction/adduction were created using a statistical analysis software package (SPSS Inc., Chicago, IL) (Equations 14 and 15).

$$AA = -0.025217*FE + 0.208808*FE^2 - 0.03981*FE^3 - 0.014949$$
 (R² = 0.985) (14)

$$IE = 0.360453*FE - 0.02316*FE^{2} - 0.034005*FE^{3} - .118174$$
 (R² = 0.991) (15)

Where

AA = Abduction/Adduction angle (radians)

IE = Internal/External rotation angle (radians)

FE = Flexion/Extension angle (radians)

The predicted correlation curves indicate a quadratic relationship between flexion/extension and abduction/adduction (Figure 37), as well as between flexion/extension and internal/external rotation (Figure 38).

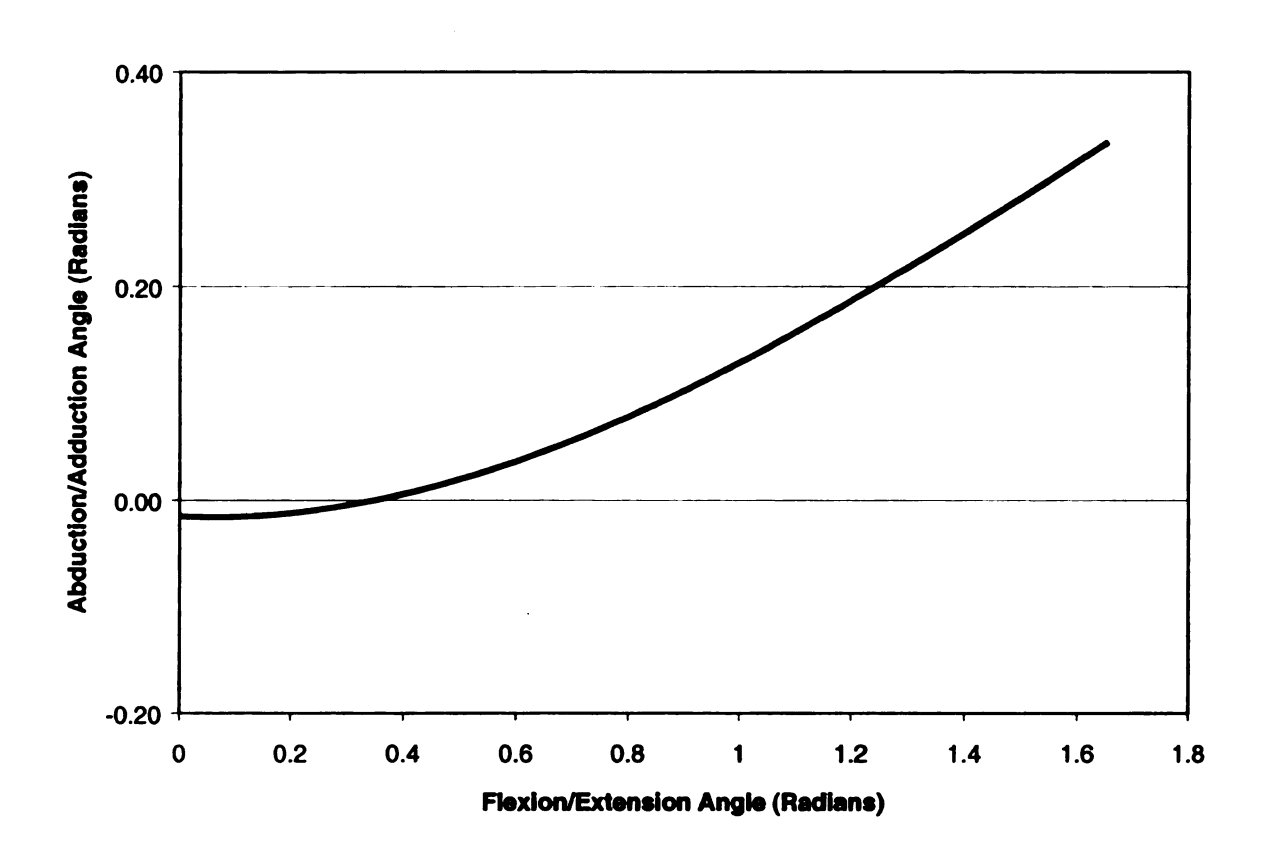


Figure 37. Predicted abduction/adduction angle vs. flexion/extension angle based on analysis of morphology of talus and tibia

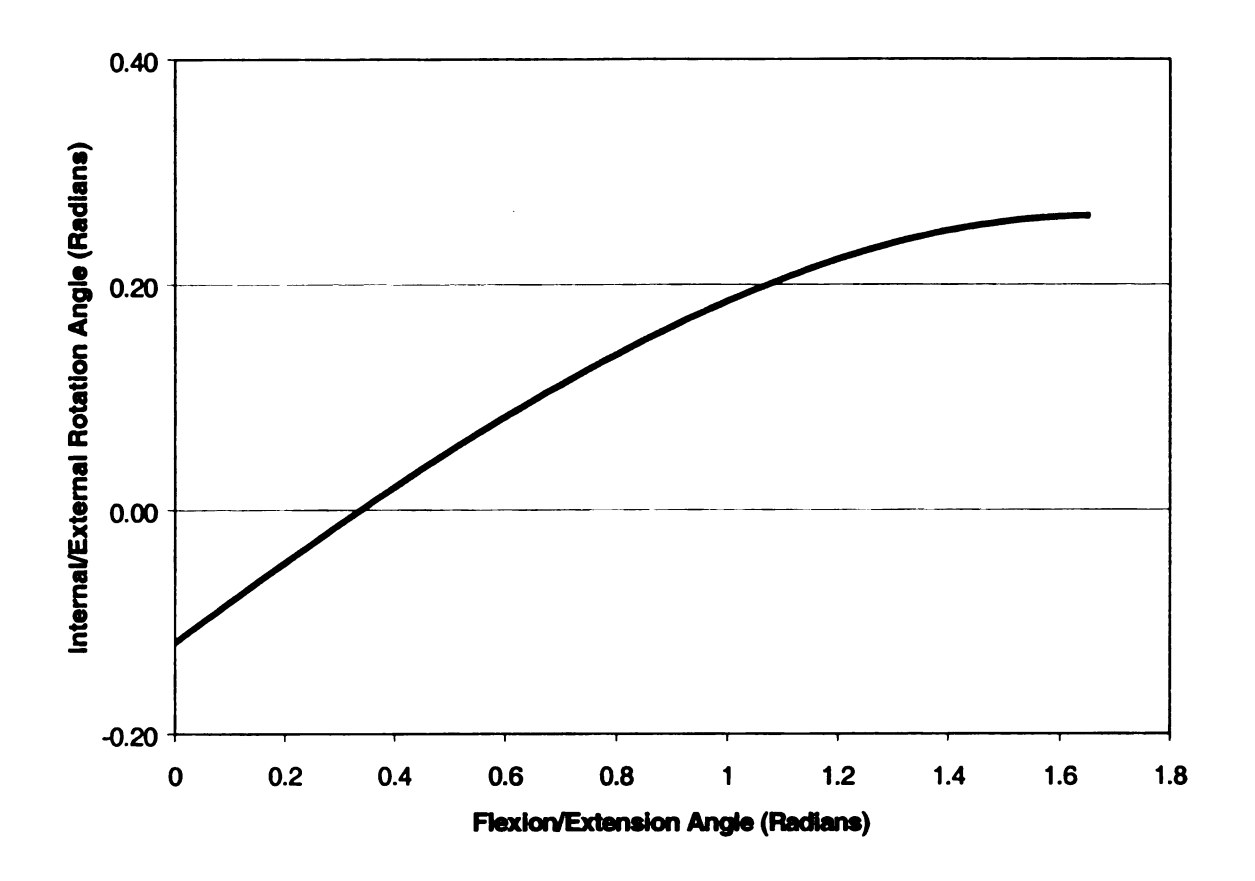


Figure 38. Predicted internal/external rotation angle vs. flexion/extension angle based on analysis of morphology of talus and tibia

These predicted results were compared to the average of five sets of kinematic data which were normalized to stance and swing phases. It should be noted that the resultant regression equation allows for only one solution for internal/external rotation and abduction/adduction for a given flexion/extension angle, due to the fact that the talar trochlea form planar curves.

4.3.1. Stance phase

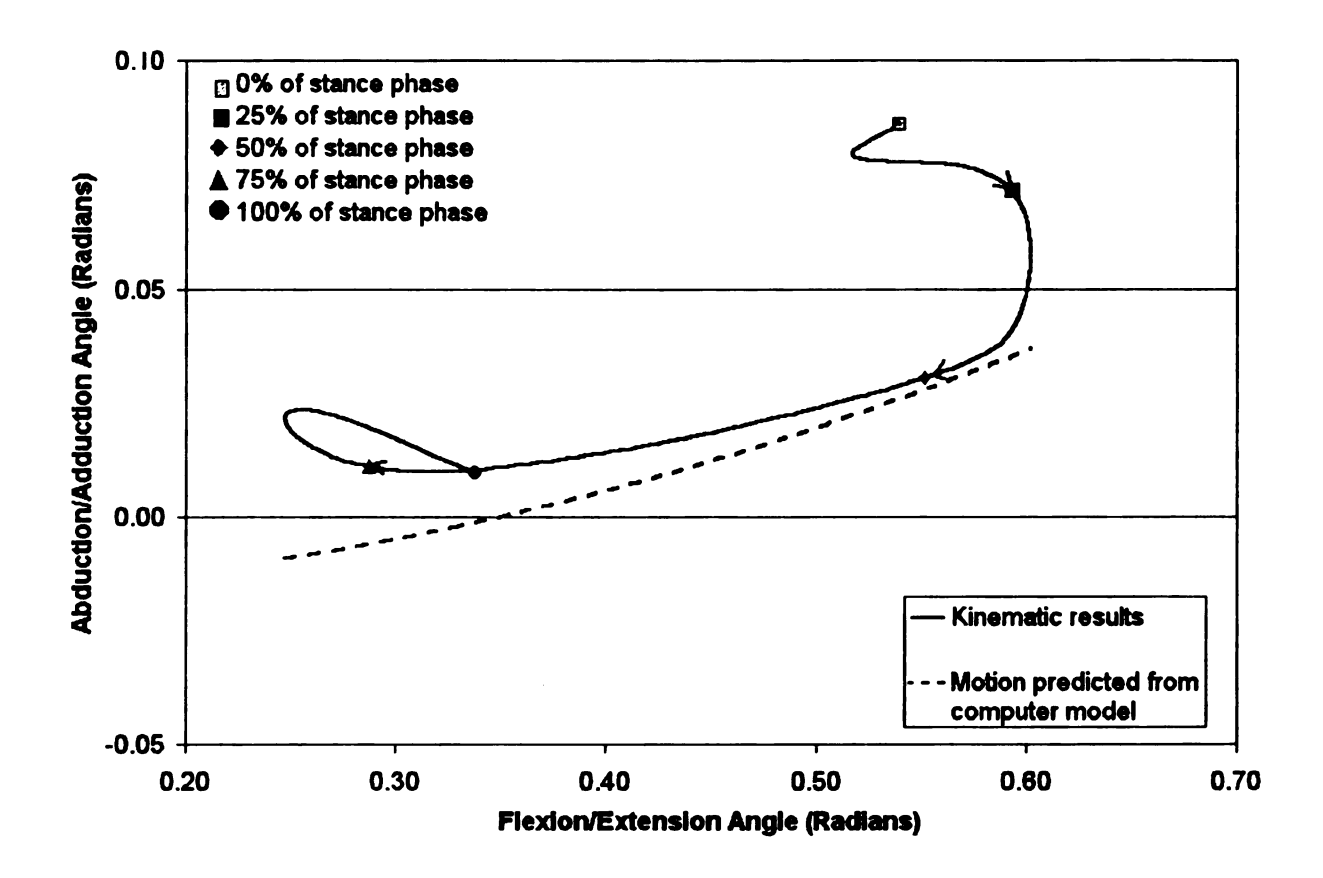


Figure 39. Flexion/extension angle vs. abduction/adduction for stance phase

The abduction/adduction of the stance phase shows a general trend of adduction throughout the stance phase (Figure 39). The range and rate of increase of adduction shown by the limb during the stance phase is similar to that predicted by the computer model. The variability in magnitudes are explained by slight variability in marker placement between the computer model and the kinematic results, or by differences in conformation between the subject used for the kinematic data collection and the development of the

computer model. Of particular importance, however, is the range of possible solutions of abduction and adduction and internal/external rotation for a given flexion extension angle. The solution derived from the computer model allows for only a single possible value of abduction/adduction or internal and external rotation for a given flexion/extension angle. Results from the experimental kinematic data analysis show a lack of a unique orientation for a given flexion/extension angle, which indicates a coupling between the solutions not taken into account by the cubic regression equations derived from the computer model.

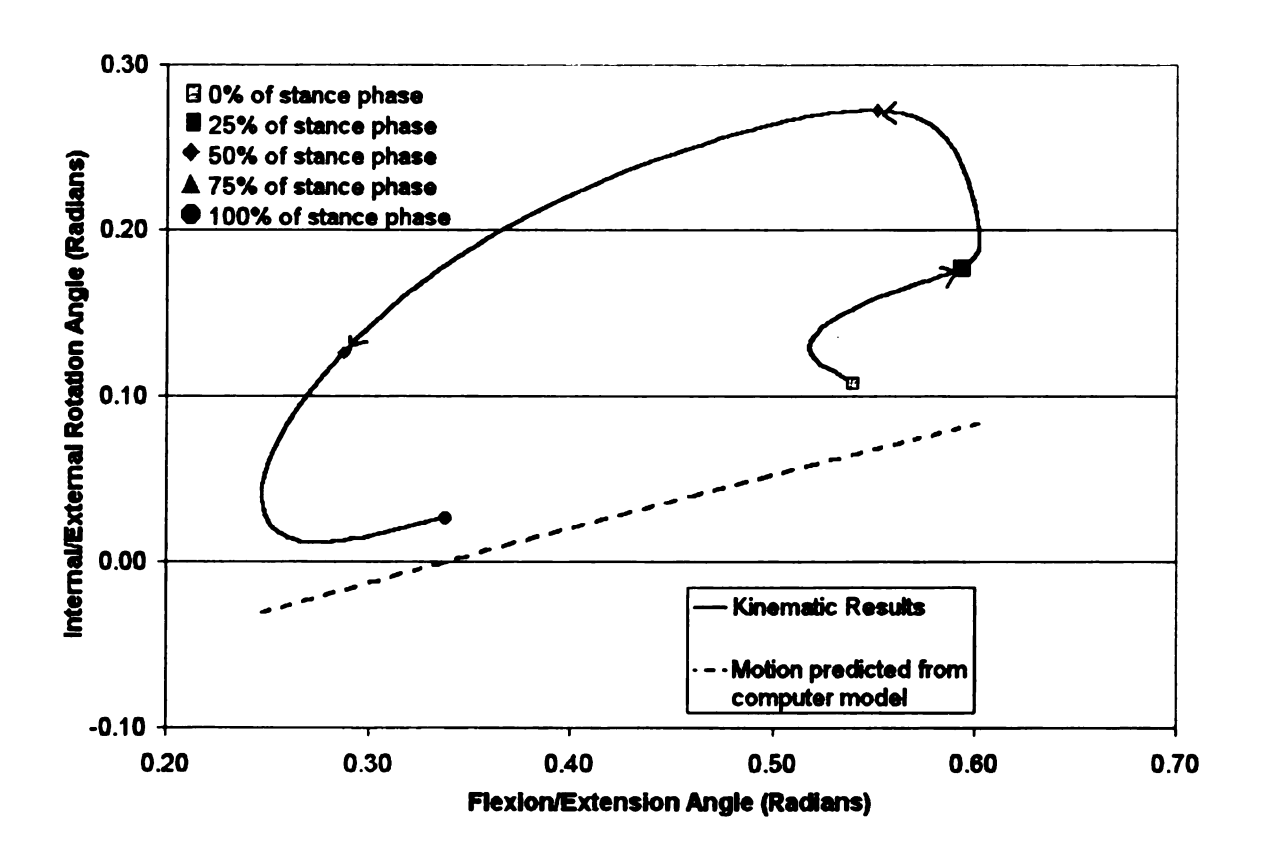


Figure 40. Flexion/extension vs. internal/external rotation for stance phase

The internal/external rotation of the limb during stance phase shows a substantial deviation from the projected results (Figure 40). The limb follows an arc that has endpoints close to those predicted by the model, but showing much greater external rotation through the duration of the weight bearing phase of the stride. The substantially greater internal rotation seen in the kinematic results suggest that the tarsal joint is twisting more under loading than would be allowed by planar rotation about the talar trochlea.

4.3.2. Swing Phase

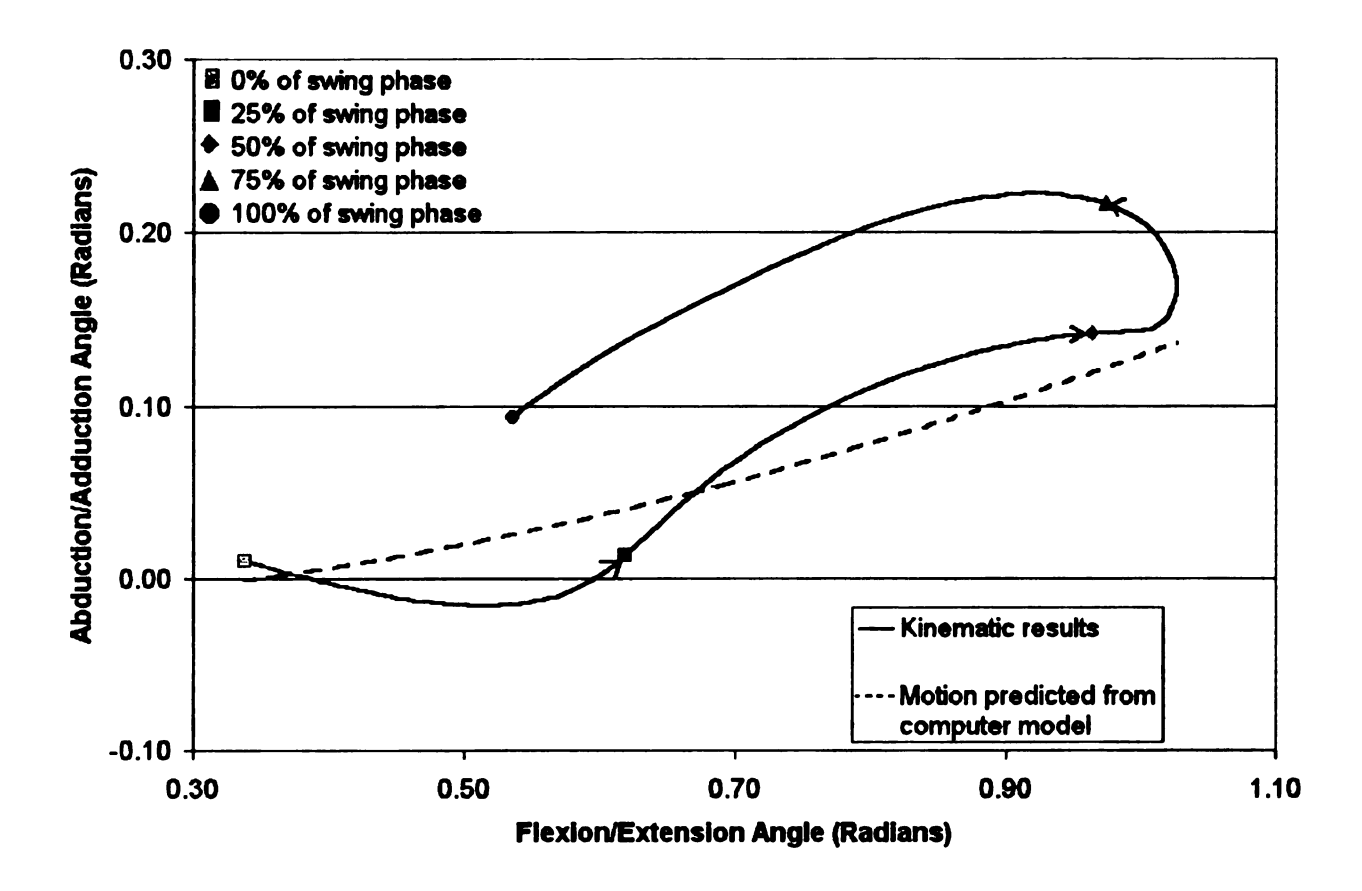


Figure 41. Flexion/extension vs. abduction/adduction angle for swing phase

The swing phase abduction/adduction angle of the limb shows a relatively close correlation to the trend of the motion predicted using the computer model (Figure 41). There is some amount of deviation, however, in that the model predicts a single possible abduction/adduction angle for a given flexion/extension angle, and the kinematics indicate that there is a consistent 0.1 radian (6°) difference between the first half and second half of swing phase.

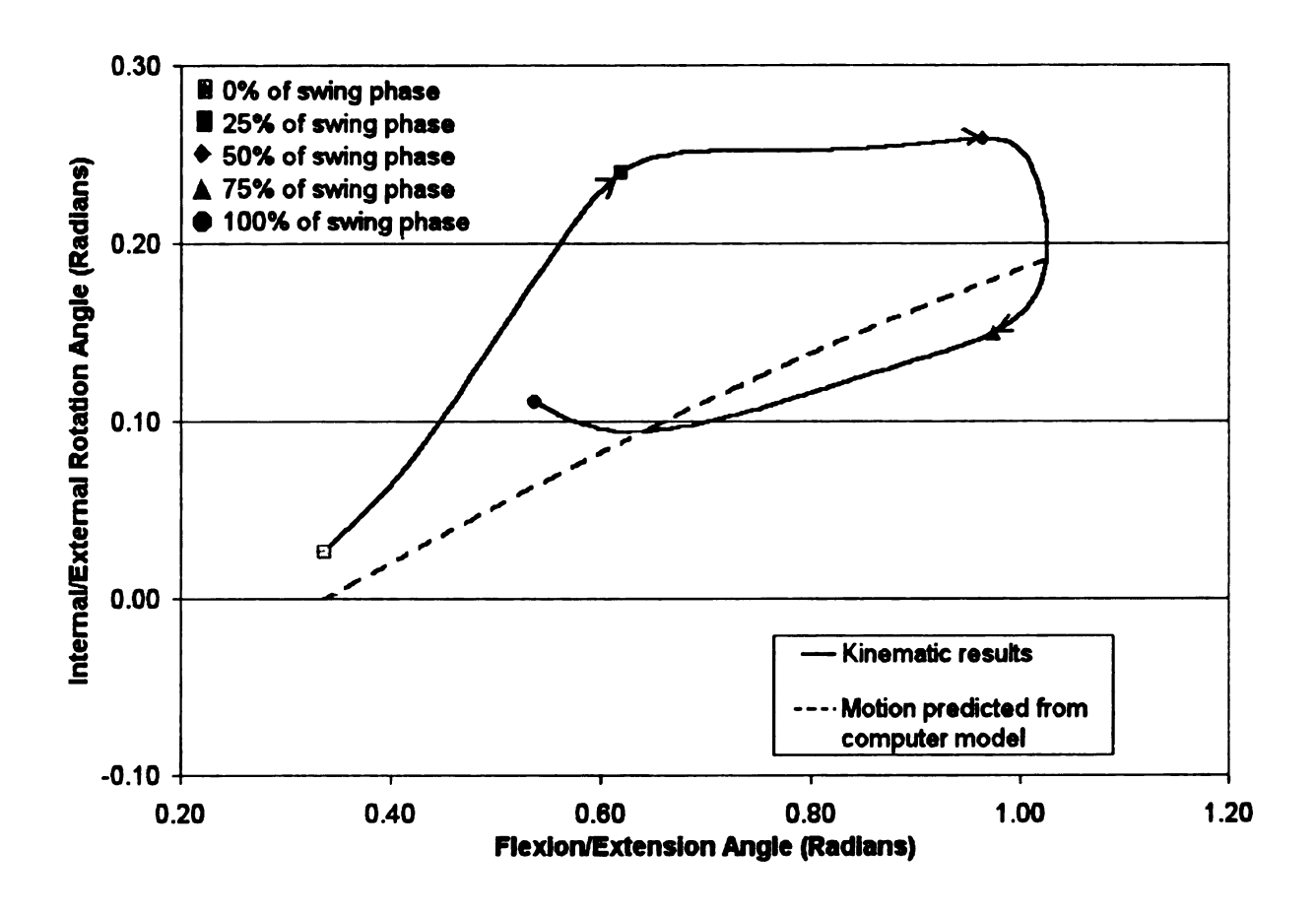


Figure 42. Flexion/extension vs. internal/external rotation for swing phase

Similarly, the internal external rotation of the limb follows the same general trends as those predicted by the morphology of the joint, but it as well demonstrates a noticeable deviation between the initial and final 50% of swing phase, whereas the predicted results state that there should be a single possible internal/external rotation angle for a given flexion/extension angle (Figure 42). The difference in this case somewhat greater, being on the order of 0.15 radians (9°).

5. Discussion

5.1. Modeling Techniques

Although no previous computer models of the tarsal joint have been developed, the techniques presented here may be compared with human and equine models of other joints. Although some unique difficulties are associated with each specific region of interest, similar issues must be addressed in almost all research into joint structure.

A number of extremely complex models have been developed focusing on the interaction of the joints in the human. The studies into the kinematics of the hand are of particular interest, as their complexity is quite similar to that of the equine tarsus. Of particular note are the studies by van sint Jan et al. (1997) and Buford and Thompson (1987). Both of these focused on three-dimensional simulation of hand biomechanics based on models derived from medical imaging data.

One of the most evident and pertinent challenges seen in almost any computer model of a physiological structure is that of raw image data resolution. The inherent limitations on image resolution from any medical imaging technique, be it CT, MRI, or ultrasound, results in the loss of surface contour that is close to the noise amplitude of the system. This was a far more profound problem in the development of the hand models, and was addressed in the case of van sint Jan et al (1997) by substantially reducing the CT scan field of view to obtain a resolution of 0.14 mm/pixel. This compares to the resolution of 0.5 mm/pixel used in this study. The lower resolution used for this study was more than compensated by the general increase in the sizes of the features of interest.

Another technique, employed by Buford and Thompson (1987), used digitized curves from radiographs performed at 10° increments. This difficult and labor intensive process was much more prone to error, and was most likely utilized simply due to the limitations on computational power and available software at that time.

This limitation in raw data is seen also in equine studies, though most structures in the horse are proportionally larger than their counterparts in the human, allowing for somewhat greater definition of 'acceptable' image resolution. The lower forelimb model (fetlock, pastern, and coffin joints) performed by Cheung and Thompson (1993) did not report a resolution, and the three-dimensional metacarpus model developed by Les et al (1997) had a 1 pixel/mm resolution. Needless to say, the definition of acceptable image

resolution is wholly dependent on the objective of the work. In the case of the study performed by Les et al (1997), the goal was the development of a finite element model of the carpus with the target being 8 node square elements of 3 mm per side. As the image data were to be 'filtered' into the finite element model, the 1 mm resolution was quite satisfactory. In the study described here, however, the objective was the development of a morphologically highly accurate model of an extremely complex joint, which necessitated a higher degree of accuracy in the image data.

A second issue pertaining to resolution for all of these studies was that of image thickness. A CT scan results in an image that is an approximation of the grayscales seen over a particular distance. This approximation means that the image, although highly accurate perhaps in the plane of the scan, may be of significantly lower accuracy normal to this plane. The study performed by Les et al (1997) used 3 mm slice thickness, Cheung and Thompson (1993) used 2 mm, and no image thickness was reported by van sint Jan et al (1997). The study reported here used the smallest image thickness available on the CT scanner being used (1.5 mm), but it also used two semi-orthogonal scans, which resulted in high resolution images in all three-dimensions. It should be noted, however, where data describing a single plane are of primary interest, such as the axis of the bone as studied by Les et al (1997), or the evaluation of hoof stresses performed by Hogan et al (1991), it is quite satisfactory to conduct scans in a single direction. This is particularly relevant when the data will be applied in the development of a finite element model, which will eliminate most of the smaller surface variations anyway.

One final issue pertaining to raw image resolution that must be of concern in all cases is the effects of radiation on live subjects. CT scans are the products of relatively high dosages of radiation due to the fact that the cross sectional images are the outcome of a series of relatively long duration and high dosage X-rays. Should a technique such as this be used on live specimens, recommended limitations on radiation exposure must be taken into account, which will inherently limit the number of scans that can reasonably be taken.

Image processing presents a far more unique challenge. This is particularly interesting, as none of the previously discussed papers (van sint Jan et al, 1997; Les et al, 1997; Buford and Thompson, 1987; Hogan et al, 1991; Cheung and Thompson, 1993) address this issue directly. Some studies, such as Buford and Thompson (1987) and Delp et al. (1990), circumvented this issue somewhat by constructing their models as hand digitized points from radiographs. This technique is extremely labor intensive and would be nearly impossible on models constructed from the inherently more accurate (due to the previously discussed issues of image resolution) CT scan images.

The use of CT scan images, however, requires some technique for edge detection and model reconstruction be employed. The lack of information on the techniques employed in the other studies prevents comparison, but the use of the Canny edge detection algorithm provided excellent data. The decision to use this technique was the product of both the common belief that it is ideal (Jahne, 1997) and a comparison with other commonly used techniques. It was evident following an analysis of techniques that the Canny algorithm (Canny, 1984) resulted in far superior edge definition than provided by other commonly used algorithms (Figures 41-46).



Figure 43. Section of original image



Figure 44. Roberts edge detection of selected region



Figure 45. Canny edge detection of selected region



Figure 46. Section of original image



Figure 47. Sobel edge detection of selected region



Figure 48. Canny edge detection of selected region

5.2. Model Validation by Volumetric Measurements

Model validation was addressed in this case by comparison of the volumetric measurements of the original specimens and reported by I-DEAS. Although this is not comprehensive in that it does not address the accuracy of the fine structure, it does serve as a gross comparison and validation of the technique.

The high degree of correlation seen between the volumetric measurements in this study indicates that the computer models do in fact, at least to the extent measurable by this technique, represent the original specimens. In actuality, however, the capacity of the software to accurately model the volume of the computer model is probably significantly higher than the resolution of the volumetric technique would allow, so the deviation between the model and its original specimen is almost certainly due to this. Increased errors seen in the case of the metatarsus and tibia are due at least to some degree to the coarse modeling technique applied to the non-articular regions of these bones. Since these regions were of lesser interest in this study, little emphasis was placed on the accuracy of the computer model outside the tarsal joint. This undoubtedly introduced additional error into the volumetric measurement.

5.3. Application of Model in the Evaluation of Tarsal Joint Kinematics

The use of the model for a kinematic examination of the statement that all tarsal joint motion occurs at the tibiotarsal joint (Schamhardt et al, 1984) was primarily to indicate the usefulness of the model in the examination of kinematic results. Kinematic analysis is used in the study of both human and animal locomotion (Soutas-Little, 1996). Although the technique is mathematically accurate, a number of assumptions are necessary for its computation.

The method is fundamentally based on the solutions of rigid body kinematics as described by Soutas-Little (1996). Although this assumption is quite accurate for the bones of the equine limb, the technique employed in this study uses retroreflective markers applied to the skin overlying bony landmarks. This introduces the possibility of the motion of the skin over the bone, which can introduce errors in the kinematic results. According to a study conducted by van Weeren (1989), skin displacement with respect to the bone on the distal end of the tibia during stance phase is negligible, and during swing phase peaks to approximately 1 cm. Skin displacement over the proximal end of the metatarsus was found to be very small throughout stance and swing.

An additional difficulty of this technique pertains to the capacity to accurately determine the three-dimensional locations of the tracked points. The tracking is performed by digitizing 60 Hz videographic image data. This technique introduces errors from the relatively low resolution of the video, as well as the possibilities of distortions introduced by lens irregularities. By averaging five strides, however, the effect of random errors was reduced, hence it may be assumed that the averaged results are generally representative of the actual motion of the limb.

The general trend of the stance phase of the abduction and adduction of the limb appears to be relatively well explained by the morphology of the tibiotarsal joint. The kinematic results in general see limited variation from the predicted motion of the joint, and what variability is seen is at least partially explained by errors introduced by the kinematic data collection process. The internal/external rotation of the limb during stance phase, however, shows much greater deviation based on the general trend of the motion of the respective segments.

For both relative rotations (internal/external and abduction/adduction), the swing phase of the limb shows variability in motion that appears to not be fully explainable simply by the motion predicted by analysis of the morphology of the talocrural/tibiotarsal joint. There is consistently a variation not only between the measured kinematic results and the results predicted using the computer model, but also in the kinematic results during swing phase for the first 50% of the stride and the return path of the final 50% of the stride. The structure of the tibiotarsal joint fails to explain this variability, and hence it is implied that there is additional motion occurring within the joint not fully explained simply by the shape of the talar ridges.

The results presented here for the motion of the metatarsus with respect to the tibia should not be taken as representative of a wide range of the equine population; they are the product of a single data collection session on a single horse. They do, however, demonstrate that the horse is capable of a great deal of motion at the tarsal joint during its normal locomotion, and there is almost certainly some coupling of motion that results in the deviation from the model based predictions.

The discrepancy between this and the results reported by Schamhardt et al (1984) could be explained in a number of ways. Small variations in internal/external rotation and abduction/adduction between the predicted and actual results can be explained by the natural morphological variation between horses, as the experimental data were taken from a different horse than the computer model was developed from. Additionally, the study performed by Schamhardt et al (1984) focused on stance phase loading and hence, although possibly accurate for the stance phase, would not accurately demonstrate the motion of the swing phase. The stance phase results could also be the product of non-axial loading not simulated in the technique described by Schamhardt et al (1984). The curvatures of the sliding intertarsal joints would explain this motion, and the technique employed by Schamhardt et al. (1984) could have inaccurately simulated the stance phase loading and hence misrepresented the amount of motion at these joints.

Another possibility that does not invalidate the conclusions drawn by Schamhardt et al (1984) is that the majority of the tarsal motion occurs at the tibiotarsal joint, but the joint between the tibia and the talus is far less rigid structure than the bone morphology would indicate. Should the bones be free to rotate slightly with respect to each other during stance, and the collateral ligaments be sufficiently dynamic as to allow for a small amount of separation during swing, it is conceivable that the out-of-plane rotations could be explained by motion occurring at the tibiotarsal joint. This is in contrast to the assertion made by Badoux (1987) that the motion of the tarsal joint is a single degree of freedom, with the talar ridges being tightly fitted into the tibial groove, preventing motion out of the plane defined by the talar trochlea. This is an unlikely explanation, however, as the additional freedom of motion between the tibia and talus would result in increased loading on limb impact and would subsequently increase the chances of degenerative joint diseases at the tarsus.

6. Conclusion and Future Studies

It is evident, based on both the visual inspection of the computer models, as well as the validation procedure conducted, that the technique described is viable for the development of computer models of equine joints for both observation of the motion, as well as for subsequent morphological studies. The models developed accurately represent the structures of the joint, and will certainly be of use for educational and research purposes.

The code developed for viewing the results of kinematic analysis in three-dimensions has proven useful in the demonstration of the research being conducted in the McPhail Lab, as well as in enhancing the general understanding of the more complex three-dimensional motions seen in certain breeds of horses by more comprehensively demonstrating their motion.

The model has also proven to be a valuable tool in the evaluation of joint kinematics. Additional analysis of tarsal joint kinematics should be conducted in order to determine the extent of variation between individuals.

Obviously it is possible to study and analyze highly complex motions centered at the tarsal joint using this technique. The disparities between the assertions of Badoux (1987) and Schamhardt et al (1984), and the findings in this study should be addressed in future research.

Subsequent studies in this field and using this technique should focus on utilization of these models for clinical and research studies. Specifically, they could be used for improving the understanding of the normal motion of the joint, as well as the process and treatment of degenerative or injury induced diseases located in the tarsus. Studies of the internal interactions of the joint by the application of bone pins or three-dimensional radiography will allow a significantly improved model of the normal motion of the equine tarsal joint.

Another area for study would be in the application of dynamic principles to more advanced models that would include the ligaments, tendons, and additional accessory structures in the hopes of developing a series of models to analyze loading through and on the joint during normal and pathological gait. Dynamic models of this type have been used in human medicine to evaluate the effects of proposed surgeries to evaluate their efficacy in improving motion prior to conducting the procedure (Sellberg and Vanderploeg, 1994). In horses, a similar technique could be employed to evaluate the value and effects on locomotion of performing fusions or tenectomies.

Finally, with a combination of the above information, accurate finite element models could be developed with certainty to their geometric accuracy and boundary conditions to evaluate the process of remodeling, fracture, and degeneration in the horse, similar to those performed in the human knee (Sathasivm and Walker, 1997), equine metacarpus (Les, et al, 1997), and equine hoof (Hogan et al, 1991). There is great potential for studies in this area having a direct and beneficial impact on the long term health and working life of the equine athlete.

References

Adams O.R., (1977) Lameness in Horses, 3rd ed, Lea and Febiger Publishing, Philadelphia, PA, pp. 318-376

American College of Radiology, National Electrical Manufacturers Association, (1993) Digital Imaging and Communications in Medicine (DICOM): Version 3.0, Draft Standard, ACR-NEMA Committee, Working Group VI, Washington, DC

Aristotle, (384-322 BC) Parts of animals; movements of animals; progression of animals. (From 1961 Edition, Eds. Peck A.L., Forster E.S. The Loeb Classical Library. London)

Badoux, D.M., (1987) Some biomechanical aspects of the structure of the equine tarsus. Anat Anz 164, 53-61

Bogert A.J. van den, Schamhardt, H.C., Crowe A., (1989) Simulation of quadrapedal locomotion using a rigid body model. *J Biomech* 22, 33-41

Buford, W.L. Jr., Thompson, D.E., (1987) A system for three-dimensional interactive simulation of hand biomechanics. *IEEE Trans Biomed Egr* **34**, 444-453

Canny, J.F., (1983) Finding edges and lines in images. M. S. Thesis, Massachusetts Institute of Technology

Chaffin, D.B., (1969) A computerized biomechanical model-Development of and use in studying gross body actions. *J Biomech* 2, 429-441

Chang, K.C., (1980) Shang Civilization, Yale University Press, New Haven, CT

Cheung T.K., Thompson K.N., (1993) Development of a three-dimensional electronic solids model of the lower forelimb of the horse. *Vet Radiol Ultrasound* 34, 331-333.

Colborne G.R., Lanovaz J.L., Sprigings E.J., Schamhardt H.C., Clayton H.M., (1998) Forelimb joint moments and power during the walking stance phase of horses. Am J Vet Res 59, 609-614

Delp S.L., Loan J.P., Hoy M.G., Zajac F.E., Topp E.L., Rosen J.M., (1990) An Interactive Graphics-Based Model of the Lower Extremity to Study Orthopaedic Surgical Procedures. *IEEE Trans Biomed Egr* 37, 757-767.

Hogan H.A., Wichtmann A.D., Hood D.M., (1991) Finite element analysis of the internal deformation and stresses in the equine distal digit. *Proc Tenth Ann Mtg Assoc Equine Sports Med, p* 43.

Jahne B., (1997) Digital Image Processing. Springer-Verlag Publishing, Berlin, Germany

Jan, S. van sint, Giurintano D.J., Thompson D.E., Rooze M., (1997) Joint kinematics simulation from medical imaging data. *IEEE Trans Biomed Egr* 44, 1175-1184

Kadletz M., (1937) Uber die bewegungsweise es tarsalgelenkes des pferds. 3. Beitrag zur Spatgenese. Arch Wissensch Prakt Tierheilk 71, 279-296

Kruger W., (1937) Ueber die schwingungen der wirbelsaule – indbesondere der wirbelbrucke – des pferds wahrend der bewgung. Berl Munchn Tierarztl Wschr 13, 197-203

Kruger W., (1938) Ueber den bewegnugsablauf an dem oberen Teil der Hintergliedmasse des pfreds im schritt, trab und galopp. *Tierarztl Rundsch* 44, 549-557

Lanovaz J.L., Clayton H.M., Colborne G.R., and Schamhardt H.C., (1999) Forelimb kinematics and net joint moments during the swing phase of the trot. *Equine Vet J Suppl* **30**, 235-240

Lanovaz J.L., Nicodemus M.N., Clayton H.M., Soutas-Little R.W., (Submitted) Virtual Targets – application of rigid body principles in equine kinematic analysis. *Am J Vet Res*

Les C.M., Keyak J.H., Stover S.M., Taylor K.T., (1997) Development and validation of three-dimensional finite element models of the equine metacarpus. *J Biomech* **30**, 737-742.

McGurk M., Amis A.A., Potamianos P., Goodger N.M., (1997) Rapid prototyping techniques for anatomical modeling in medicine. *Annals Royal Coll Surg England* 79, 169-174.

Moskovits S., (1930) Die statisch-mechanische beurteilung der arbeitstiere durchgefuhrt am metacarpus der pferde. Wiss Land Abt Tiern Tierz 2, 372-421

Pasquini, C., Reddy V. K., Ratzlaff M., (1978) Atlas of Equine Anatomy, Sudz Publising, Albion, WA

Pluvinel, Antoine de, (1626) Le Meanege Royal, (From 1989 Edition. Ed. Nelson, H. JA Allen & Co. Ltd. London)

Remmler D., Olson L., Ekstrom R., Duke D., Matamoros A., Matthews D., Ullrich C.G., (1998) Pre-surgical CT/FEA for craniofacial distraction: I. Methodology, development, and validation of the cranial finite element model. *Med Eng Phys* 20, 607-619

Rossdale, P.D., Hopes, R., Wingfield Digby, N.J., Offord, K., (1985) Epidemiological study of wastage among racehorses 1982 and 1983. *Vet Rec* 116, 66-69

Sathasivam S., Walker P.S., (1997) A computer model with surface friction for the prediction of total knee kinematics. *J Biomech* 30, 177-184

Schamhardt H.C., Hartman W., de Lange A. (1984) Kinematics of the equine tarsus. Abstracts of the XV Congress of the European Association of Veterinary Anatomists, Utrecht, The Netherlands

Schnuck B.G., (1986) Gaussian Filters and Edge Detection. General Motors Research Laboratories Research Publication, Warren, Michigan

Sellberg M.S., Vanderploeg, M.J., (1994) Virtual human: a computer graphics model for biomechanical simulations and computer-aided instruction. *IEEE Trans Biomed Egr* **6**, 329-330

Soutas-Little, R.W., (1996) The use of virtual markers in human movement analysis. *Gait Post* 4, 176-177

Thompson, K.N., Cheung, T.K., (1994) A finite element model of the proximal sesamoid bones of the horse under different loading conditions. *Vet Comp Othop Traumatol* 7, 35-39

Tsumura, H., Miura, H., Iwamoto, Y., (1989) Three-dimensional pressure distribution of the human hip joint – comparison between normal hips and dysplastic hips. Fukouka Igaku Zasshi 89, 109-118

van Weeren P.R., (1989) Skin Displacement in Equine Kinematic Gait Analysis. Ph.D. Thesis, Utrecht, The Netherlands

van Weeren, P.R., (In Press) History. In: *Equine Locomotion*. Eds. Back, W. Clayton, H.M., W.B. Saunders, London, England

Weichert R., (1927) Messungen an ostpreuvischen kavalleriepferden und solchen mit besonderen leistungen und die beurteilung der leistungsfahigkeit auf grund der mechanischen verhaltinesse. Arb Deutsch Ges Zuch 34, 1-67

Whittle M., (1991) Gait Analysis, an introduction. Butterworth-Heinemann, Ltd, Oxford, England

Xenophon, De Re Equestri, 380 B.C. (from 1942 edition. Ed. Dakyns, G.H., Random House)

